

This is the author's final, peer-reviewed manuscript as accepted for publication (AAM). The version presented here may differ from the published version, or version of record, available through the publisher's website. This version does not track changes, errata, or withdrawals on the publisher's site.

Experimental and computational studies of sulfided NiMo supported on pillared clay: catalyst activation and guaiacol adsorption sites

F. Oemry, I. B. Adilina, W. T. Cahyanto, N. Rinaldi, F. Aulia,
A. Jackson, S. F. Parker, A. B. Kroner, E. J. Shotton

Published version information

Citation: F Oemry et al. 'Experimental and computational studies of sulfided NiMo supported on pillared clay: catalyst activation and guaiacol adsorption sites'. Phys Chem Chem Phys (2023).

DOI: [10.1039/D2CP03987G](https://doi.org/10.1039/D2CP03987G)

This version is made available in accordance with publisher policies. Please cite only the published version using the reference above. This is the citation assigned by the publisher at the time of issuing the AAM. Please check the publisher's website for any updates.

This item was retrieved from **ePubs**, the Open Access archive of the Science and Technology Facilities Council, UK. Please contact epublications@stfc.ac.uk or go to <http://epubs.stfc.ac.uk/> for further information and policies.

PCCP

Physical Chemistry Chemical Physics

Accepted Manuscript

This article can be cited before page numbers have been issued, to do this please use: F. Oemry, I. B. Adilina, W. T. Cahyanto, N. Rinaldi, F. Aulia, A. J. Jackson, S. F. Parker, A. Kroner and E. J. Shotton, *Phys. Chem. Chem. Phys.*, 2022, DOI: 10.1039/D2CP03987G.



This is an Accepted Manuscript, which has been through the Royal Society of Chemistry peer review process and has been accepted for publication.

Accepted Manuscripts are published online shortly after acceptance, before technical editing, formatting and proof reading. Using this free service, authors can make their results available to the community, in citable form, before we publish the edited article. We will replace this Accepted Manuscript with the edited and formatted Advance Article as soon as it is available.

You can find more information about Accepted Manuscripts in the [Information for Authors](#).

Please note that technical editing may introduce minor changes to the text and/or graphics, which may alter content. The journal's standard [Terms & Conditions](#) and the [Ethical guidelines](#) still apply. In no event shall the Royal Society of Chemistry be held responsible for any errors or omissions in this Accepted Manuscript or any consequences arising from the use of any information it contains.

Experimental and Computational Studies of Sulfided NiMo Supported on Pillared Clay: Catalyst Activation and Guaiacol Adsorption Sites

Received 00th January 20xx,
Accepted 00th January 20xx

DOI: 10.1039/x0xx00000x

F. Oemry,^{*a} I. B. Adilina,^b W. T. Cahyanto,^c N. Rinaldi,^b F. Aulia,^b A. Jackson,^d S. F. Parker,^e A. B. Kroner,^f E. J. Shotton^f

We report on intermediate (oxysulfides) and sulfided structures of NiMo supported on aluminium pillared clay (Al-PILC) during the catalyst activation process and the preferred guaiacol adsorption sites on the sulfided catalyst. *In situ* X-ray absorption fine structure (XAFS) together with density functional theory (DFT) calculations confirm the existence of ill-defined suboxides (MoO_x, NiO_x) and the well-known subsulfides (Mo₂S₉, Ni₃S₂) at the first stage which, at a later stage in the process, transform into MoS₂ with two edges, oxygen-decorated Mo and Ni with zero sulfur coverage. The freshly sulfided NiMoS₂ catalyst under sulfiding agents is mainly terminated by Mo-edge surface with 50% sulfur coverage (Mo-S50) with a disordered Ni-edge surface that can be assigned as NiMoS (1010). When exposed to an inert atmosphere such as He gas, the Mo and Ni edges evolved partially into new structures of Mo and Ni edges with zero sulfur coverage, labelled as Mo-Bare and Ni-Bare. Guaiacol is often used as a model compound for lignin and a series of calculations of guaiacol on the structural edges of a sulfided NiMoS₂ catalyst show relatively good agreement between the observed and calculated inelastic neutron scattering (INS) spectra for Mo-S50, Ni-Bare, and NiMoS (1010) where guaiacol weakly chemisorbed via oxygen atom of OH group. The results also confirm that guaiacol is physisorbed on the basal plane of NiMoS₂ in a horizontal (flat-lying) configuration via van der Waals interaction at a separation of about 3.25 Å.

1. Introduction

Biofuels have emerged as one of the solutions to address the growing energy demands of the transportation sector. Most biofuels available in the market are obtained from food crop based feedstocks produced using well-established technologies.¹ However, agricultural wastes provide a more sustainable source of lignocellulose, a key component in second generation biofuel production.^{2,3} One prospective method for biofuel production is conversion of lignocellulose into bio-oil via fast pyrolysis and then upgrading the bio-oil over a catalyst, to remove oxygen as H₂O (hydrodeoxygenation, HDO).^{3,4} Supported metal sulfides (e.g. NiMoS, CoMoS),^{5,6} noble metals (e.g. Ru, Rh, Pd and Pt),^{6,7} and base metals (e.g. Fe, Ni and Cu)^{8–10} have been widely adopted as active metals in HDO catalysts. However, the deactivation of these catalysts during the HDO reaction is still an inevitable degradation process and is frequently observed in many industrial applications.^{11–13} The most common causes are catalyst poisoning by water and

oxygen,^{13–15} catalyst sintering,^{16,17} and active site blockage by alkali metals and/or carbon deposition.^{18–20}

As a result of the issues described above, we have developed a bentonite-based aluminium pillared interlayer clay (Al-PILC) as a new alternative support for NiMoS₂ catalysts. This was encouraged by early reports that show silica-based supports are less susceptible to the formation of strongly bound phenates, which are known coke precursors, one of the leading causes for the deactivation of the catalysts supported on alumina.^{21,22} The studies noted that the presence of Lewis acid-base pairs on the alumina surface, makes the surface particularly reactive toward oxygenated compounds. On the other hand, the acidity of PILC can be fine-tuned by simply changing the type of pillaring agents^{23,24} and hence there is a reasonable grounds to consider Al-PILC as a potential HDO catalyst support. In a previous study, we have demonstrated that the NiMoS₂/Al-PILC catalyst was able to convert 100% guaiacol (2-methoxyphenol, GUA, a lignin model compound) with high selectivity, producing 77% of phenol as the major HDO product.²⁵ The infrared (IR) and inelastic neutron scattering (INS) spectra suggest that GUA conversion to phenol was initially preceded by GUA adsorption on the sulfided catalyst via H-bonding interactions. However, further work is still needed to properly translate these IR and INS spectra into accurate structural models of GUA-NiMoS₂ at the atomic scale.

Several density functional theory (DFT) studies have explored how oxygenated and sulfur compounds are adsorbed on NiMoS₂ and CoMoS₂ catalysts.^{26–29} The active sites of the promoted catalysts that act as adsorption sites for both oxygenated and sulfur compounds have been associated with the edges of the catalysts rather than their basal planes. Based on scanning tunnelling microscopy (STM) and scanning transmission electron microscopy (STEM), from which the DFT studies were derived,^{30–35} the hexagonal shape of CoMoS₂ is terminated by alternating Mo and Co edges with some degree

^a Research Center for Quantum Physics, National Research and Innovation Agency, Kawasan Puspiptek Serpong, Tangerang Selatan, Banten 15314, Indonesia
Email: fere001@brin.go.id

^b Research Center for Advanced Chemistry, National Research and Innovation Agency, Kawasan Puspiptek Serpong, Tangerang Selatan, Banten 15314, Indonesia

^c Department of Physics, Universitas Jenderal Soedirman, Jl. dr. Soeparno 61, Purwokerto 53122, Indonesia

^d Scientific Computing Department, STFC Rutherford Appleton Laboratory, Chilton, Didcot, Oxfordshire OX11 0QX, United Kingdom

^e ISIS Neutron and Muon Source, STFC Rutherford Appleton Laboratory, Chilton, Didcot, Oxfordshire OX11 0QX, United Kingdom

^f Diamond Light Source Ltd, Diamond House, Harwell Science and Innovation Campus, Didcot, Oxfordshire, OX11 0DE, United Kingdom

[†] Electronic Supplementary Information (ESI) available: [details of any supplementary information available should be included here]. See DOI: 10.1039/x0xx00000x

of sulfur coverage. The structure of NiMoS₂ is more complicated, as its final structure is highly sensitive to the annealing temperature during catalyst activation. In general, NiMoS₂ is mainly composed of larger NiMoS type A (a truncated hexagonal shape) and smaller NiMoS type B clusters (a complex dodecagonal shape), where NiMoS type B accounts for 77 % and 54% of the nanocluster size distribution at after annealing at temperatures of 673 K and 773 K, respectively.^{31,32} Since NiMoS₂/Al-PILC was prepared and sulfided at temperatures below 673 K,²⁵ disordered NiMoS type B is presumed to be the dominant structure, as compared to the well-ordered NiMoS type A but this conjecture needs to be tested. Therefore, knowing the local structure of Mo- and Ni-edges on fresh NiMoS₂/Al-PILC catalyst becomes a prerequisite in order to increase the accuracy of models adopted in DFT calculations to properly decode the IR and INS spectra of adsorbed GUA into structural models, that can be used as a basis to scrutinize feasible reaction paths for the GUA-to-phenol transformation.

X-ray absorption fine spectroscopy (XAFS) has been applied successfully in the past to characterize several variants of CoMoS₂/Al₂O₃ and NiMoS₂/Al₂O₃ catalysts to understand the local structure of Mo and Ni (or Co) atoms and how those promoter atoms (Ni or Co) are distributed in the MoS₂ template.^{36–40} Although *in situ* XAFS measurements in the past have been reported to give reliable information on the MoS₂ morphology,^{41,42} previous XAFS studies on NiMo catalysts have mainly focussed on the oxide-to-sulfide transformation, doping and aging effects without further elaborating a representative portrait of how the Ni- and Mo- atoms are actually distributed at the edges of the catalysts. In contrast to STM or STEM studies, no previous XAFS study has proposed structural models to describe the atomic arrangement of Mo- and Ni-edges on a fresh NiMoS₂ catalyst.

In the present work, *in situ* XAFS measurement on NiMoS₂/Al-PILC was conducted to validate DFT-based NiMoS₂ models that could best describe the atomic arrangement of its Mo- and Ni-edges. The structural models obtained from extended X-ray absorption fine structure (EXAFS) fitting procedures serve as inputs to DFT calculations to investigate the preferred adsorption sites for GUA. The most stable configurations of adsorbed GUA on NiMoS₂ are determined from its adsorption energy and the calculated vibrational spectra of GUA in each stable configuration can be directly compared to IR and INS data from our previous work.²⁵ Here, we demonstrate that a combined XAFS and DFT study, assisted by earlier INS data, have led to a better understanding of how GUA is adsorbed on Mo- and Ni-edges on NiMoS₂/Al-PILC.

2. Experimental and computational details

2.1 Materials and synthesis

Aluminium chloride, ammonium heptamolybdate tetrahydrate, nickel nitrate hexahydrate and sodium hydroxide were obtained from Merck. Bentonite clay (BT, surface area: 208 m²g⁻¹) was purchased from Sigma–Aldrich and used as a precursor for the pillared clay catalyst support. Detailed information of

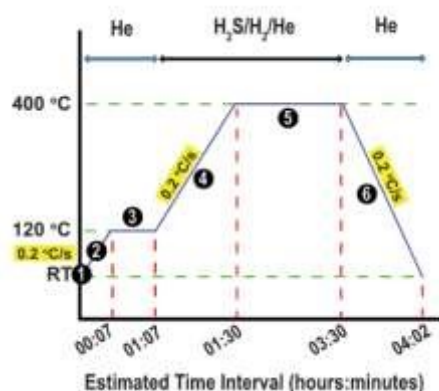
the Al-PILC synthesis can be found in our previous work.²⁵ Al-PILC supported NiMo catalysts were synthesised by loading ammonium heptamolybdate and nickel nitrate hexahydrate using a double impregnation method. After each impregnation, the catalyst was dried at 333 K overnight and calcined at 773 K for 5 h in static air resulting in the catalyst precursor in an oxide form denoted as NiMoPILC.

2.2 *in situ* XAFS, MS, and HRTEM measurements

XAFS studies on calcined NiMoPILC were carried out on the B18 beamline at the Diamond Light Source at Harwell, United Kingdom.⁴³ The storage beam energy was 3 GeV and the ring current 300 mA. Mo K-edge spectra (in the range of 19,800 to 20,800 eV) were collected in transmission mode using ion chamber detectors with a fast scanning Si(111) double crystal monochromator, with a Mo foil placed between I_t and I_{ref}. Ni K-edge XAS data were collected in fluorescence-yield mode using a 36 element Ge detector. The elastic scattering contribution was minimised by placing the detector at 90° to the incoming beam, with the sample oriented at 45° to the incoming beam. X-ray beam dimensions at the sample position were 1×1 mm². The acquisition of each spectrum took ~120 s. *In situ* experiments were performed using a setup developed by Kroner et al.⁴⁴ For the experiments, 40 mg of the as-prepared catalysts (sieve fractions: 0.425–0.150 mm) were placed in a 3 mm diameter quartz capillary. Prior to activation, the sample was heated using a hot gas blower under He gas flow (heating rate = 0.2°C/min). Scheme 1 describes the plan for temperature and gas flow treatment during *in situ* Mo K-edge and Ni K-edge XAFS measurements as a function of time which consists of six stages: 1 - starting point of the experiment, 2 – heating to 120 °C under He gas; 3 – drying at 120 °C under He gas; 4 – heating to 400 °C under H₂S/H₂/He gases; 5 - sulfidation at 400 °C under H₂S/H₂/He gases; 6 – cooling to room temperature (RT) under He gas. A mixture of H₂S/H₂ gases in He gas carrier (1% H₂S, 9% H₂, 90% He) at atmospheric pressure was flowed through the dried NiMoPILC in the *in situ* catalytic cell as it was heated from 120 °C to 400 °C at a rate of 10 mL/min. XAFS data was collected during the heating ramp as well as while cooling to room temperature and at each stage of the sulfidation. The Ni K-edge data were recorded, the sample was then replaced by a fresh sample from the same batch of catalyst and the Mo K-edge data recorded using the same procedure as for the Ni K-edge data (Scheme 1). XAFS data analysis was performed using the Demeter software package.⁴⁵ EXAFS data fitting to model spectra was done using an amplitude reduction factor of 0.90, which was obtained by fitting the Mo and Ni foils reference to crystallographic data from the ICSD database,⁴⁶ which also include NiO (ICSD-9866), Ni₃S₂ (ICSD-23114), MoS₂ (ICSD-24000), MoO₃ (ICSD-35076), and α-NiMoO₄ (ICSD-81059). The k-range values used in the fitting were 3 - 11 Å⁻¹ for the Mo K-edge and 2.8 - 12 Å⁻¹ for the Ni K-edge whereas the R range spanning between 1 and 4 Å was used. The Mo K-edge and Ni K-edge positions were taken as the energy at half-step height. The Fourier transformed (FT) EXAFS data presented are not phase corrected.⁴⁵ In addition, mass spectroscopy (MS) was also

employed to qualitatively trace and analyse vapor gases that exited the reactor cell outlet in real time. The MS measurement serves as a guidance for EXAFS data interpretation in terms of the consumption and production of gases by NiMoPILC catalyst (Fig. 1S, ESI[†]).

The morphology of fresh sulfided NiMoS₂/Al-PILC was examined by high-resolution transmission electron microscopy (HR-TEM) operated at 200 keV using a LaB₆ filament on a Tecnai G² 20 S-TWIN at the BRIN research facility in Serpong, Indonesia. The powder samples were ultrasonically dispersed in an ethanol solution under ambient atmosphere and deposited through drop-casting on a carbon film supported by a 200 mesh gold TEM grid. The slab lengths of the sulfided NiMoPILC were estimated using ImageJ software.⁴⁷



Scheme 1. Temperature and gas flow treatment during *in situ* Mo K-edge and Ni K-edge XAFS measurement which are categorized into successive treatment stages 1-6.

The INS spectrum of NiMoS₂/Al-PILC dosed with GUA used in this present study was from our previous work.²⁵ In brief, the catalyst pre-treatment for INS measurement consisted of packing the catalyst samples (ca. 20 g) into a stainless steel or Inconel can and drying under a flow of helium gas at 473 K for 2 h. GUA (0.7 – 0.9 mmol (g catalyst)⁻¹) was then loaded into the catalyst at room temperature in a gas line by heating GUA into the gas phase at 413 K under 60 mL min⁻¹ flowing helium, to give the GUA-adsorbed catalyst (dosed samples).

2.3 Computational details

DFT calculations were used to reconstruct both MoS₂ and the edges of NiMoS₂ structures, which were later converted to crystallographic information file (CIF) inputs for IFFFIT calculations using the Artemis software.⁴⁵ The calculations were performed using VASP (Vienna Ab Initio Simulation Package).^{48,49} We applied the generalized gradient approximation (GGA) with the Perdew-Wang (PW91)^{50,51} exchange correlation functional and the projector augmented wave (PAW)⁵² method by implementing a plane-wave cut-off energy of 400 eV. Supercell's Brillouin zone integral was calculated by special *k*-point samples developed by Monkhorst and Pack⁵³ using a 1 × 3 × 1 grid. Ionic relaxation was carried out until the Hellmann-Feynman forces on each atom were less than 0.01 eV/Å. For the purpose of EXAFS data fitting analysis, single-layer 3x3x1 supercell models were simulated in a

parallelogram box with dimension of 27.6 × 9.45 × 15.3 Å where the supercells are repeated with a periodicity of 21 Å perpendicular to the edge surface (*x*-direction) and 12 Å perpendicular to MoS₂ or NiMoS₂ planes (*z*-direction). The distances were chosen to be large enough to ensure the interactions between chains can be neglected. For the Mo₂S₉ cluster case, a cubic box with sides of 18 Å and gamma *k*-points were adopted. Only one Mo atom was fixed and the remaining atoms were relaxed. The single-layer models which matched the EXAFS data were expanded into multilayer MoS₂ and NiMoS₂ structures and reconstructed in a 4x4x1 supercell of 27.6 × 12.6 × 12.3 Å following previous STEM and DFT studies.^{26,35} The reconstruction of multilayer MoS₂ and NiMoS₂ models is also based on HRTEM images (see Fig. 2S, ESI[†]) that confirms NiMoS₂ catalyst supported on Al-PILC support has a stacked multilayer structure with average slab length of 6–8 nm. For the calculation of GUA adsorption on MoS₂ and NiMoS₂ edge surfaces, all GUA atoms and adjacent atoms on the two upper rows of the surface edges were allowed to undergo full relaxation while the remaining atoms were fixed. For GUA adsorption on the basal plane (0001) of multilayer MoS₂, a 4x4x1 supercell of 12.6 × 12.6 × 25 Å was adopted, which has four MoS₂ units in the *x*- and *y*-directions. The slabs are separated by 15.75 Å in the *z*-direction. A *k*-point mesh 3x3x1 was chosen to give an accurate sampling of the Brillouin zone. The calculation was carried out including van der Waals (vdW) interactions using the DFT-D3 functional as implemented in VASP. The GUA adsorption energy (E_{ads}) is calculated from the total energy difference between multilayer MoS₂ or NiMoS₂ surface with GUA ($E_{\text{surface+GUA}}$), multilayer MoS₂ or NiMoS₂ surface (E_{surface}), and isolated GUA (E_{GUA}) as given by the equation, $E_{\text{ads}} = E_{\text{surface+GUA}} - (E_{\text{surface}} + E_{\text{GUA}})$. Vibrational transition energies of GUA were calculated from the optimized structures by displacing each atom of guaiacol from its equilibrium position using the finite difference method implemented within VASP. The VASP output includes the vibrational transition energies and the atomic displacements of the atoms in each mode. The latter provides visualization of the modes using Chemcraft⁵⁴ and also serves as the input for the AbINS program⁵⁵ that simulates the INS spectrum for TOSCA (the instrument used to record the INS spectra,²⁵ i.e. the instrument geometry and broadening effects are included). A “nightly” build of Mantid⁵⁶ (01/23/45) was used to access recent updates to AbINS. These are due for release in Mantid 6.2.0.

Results and Discussion

3.1. XANES and degree of sulfidation

Fig. 1 shows *in situ* Mo K-edge and Ni K-edge XANES spectra for all stages including catalyst activation (stages 4-5) of NiMoPILC. For the Mo K-edge case, both MoO₃ and α-NiMoO₄ spectra possess similar pre-edge features but different post-edge profiles: the MoO₃ spectrum tends to be dampened, while α-NiMoO₄ spectrum first rallies to the reversal point at E₂ and then oscillating around the equilibrium position. Careful examination reveals that the NiMoPILC spectra at stages 1 and 2 more clearly

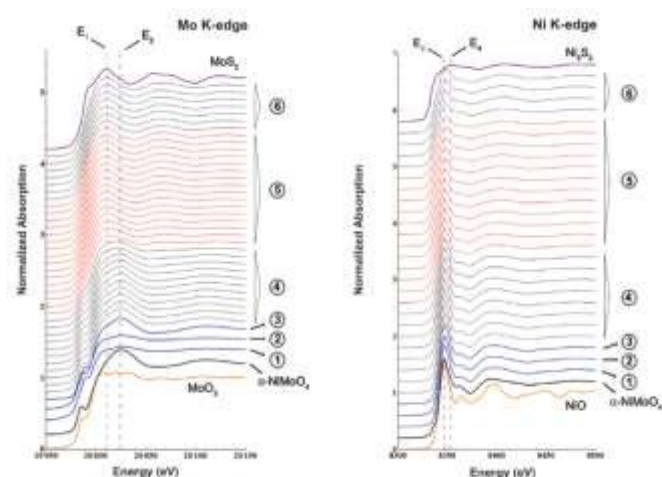


Fig. 1 in situ Mo K-edge (left) and Ni K-edge (right) XANES spectra of NiMoPILC at varying temperatures and gas composition. Vertical dashed lines represent global maximum peaks of MoS_2 ($E_1 = 20010.84$ eV) and $\alpha\text{-NiMoO}_4$ ($E_2 = 20024.35$ eV) in the Mo K-edge data and $\alpha\text{-NiMoO}_4$ ($E_3 = 8346.27$ eV) and Ni_3S_2 ($E_4 = 8353.02$ eV) in the Ni K-edge XANES regions. The numbers correspond to the successive treatment stages that are defined in Scheme 1.

resemble that of the MoO_3 reference prior to heat treatment at 120°C (stage 3). Only after NiMoPILC underwent a considerable drying process did the spectrum gradually transform into that of the $\alpha\text{-NiMoO}_4$ reference. However, this behaviour cannot be found in the NiMoPILC spectra at stages 1-3 for the Ni K-edge case, where the spectra and that of the $\alpha\text{-NiMoO}_4$ reference are alike. We argue that spectral discrepancy observed in stages 1-3 for the Mo K-edge case is caused by trapped water molecules within $\alpha\text{-NiMoO}_4$ structure which cause a slightly distorted local structure of surrounding Mo atoms as confirmed by MS measurement (Fig. 1S, ESI⁺) where a predominant peak rise at stages 1-3 was detected due to water release but less pronounced for the Ni K-edge case.

At the beginning of the sulfidation process of the stage 4-5 period, we could discern a continuous peak shift of the Mo K-edge XANES spectra from E_2 to E_1 , which indicates a gradual structural transformation from $\alpha\text{-NiMoO}_4$ to MoS_2 . Meanwhile, the Ni K-edge XANES spectra only demonstrate an intensity reduction of the white line without any visible peak displacement from E_3 to E_4 . This could be interpreted as the local Ni structure of sulfided NiMoPILC not corresponding to that of the Ni_3S_2 reference. The absence of the Ni_3S_2 phase indicates no significant Ni sulfide segregation occurred, unlike as is normally observed in commercial alumina-based catalysts.⁵⁷ In addition, the further peak shifting and white line intensity reduction observed in the Mo K-edge, along with no changes detected for the Ni K-edge XANES spectra at stage 6, indicates that major structural change only occurs during the sulfidation process. To clarify this observation, we replot the XANES spectra for stages 4-5 as stacked lines and portray them in Fig. 2(a and b). Here, we show that the black (stage 4) and red (stage 5) lines intertwine at some points marked by arrows for both the Mo K-edge and Ni K-edge cases. These isosbestic points are usually interpreted as a sign of two phases that co-exist during a phase transition.⁵⁸ To confirm whether stages 4-5 have two phases or not, we performed additional investigations using principal component analysis (PCA) as implemented in the

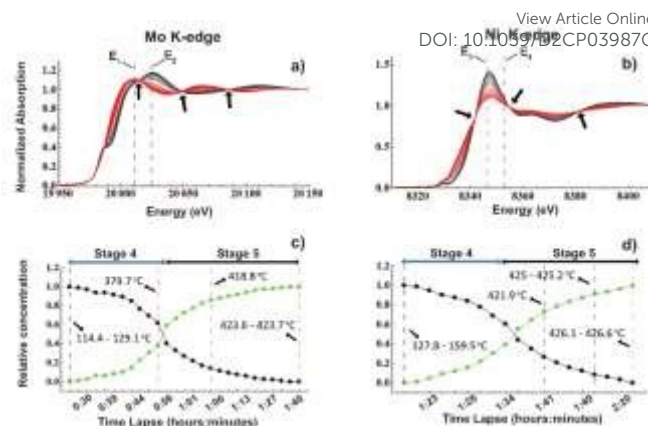


Fig. 2 Normalized XANES spectra of NiMoPILC at stages 4-5 (a, b) and their corresponding degree of molybdenum and nickel sulfidation as determined by ITFA (c, d). In (a) and (b), the arrows in the normalized XANES spectra of stages 4-5 indicate positions of isosbestic points, while the black and green lines and points in c) and d) represent $\alpha\text{-NiMoO}_4$ and NiMoS_2 , respectively.

Iterative Target Transformation Factor Analysis (ITFA) software.^{59,60} PCA is used to identify how many components (phases) are embodied in the investigated structure. This information is useful for EXAFS fitting analysis when deciding how many structural models are needed for FEFF calculations. Note that in addition to PCA, ITFA can also measure the percentage concentration of each component that contributes to the spectra. Fig. 2(c and d) show ITFA-based relative concentration data corresponding to each of the XANES spectra in Fig. 2(a and b). The existence of two phases in stages 4-5, suggested by the presence of isosbestic points in Fig. 2(a and b), has been substantiated by a clear trend in Fig. 2(c and d) where one phase completely transforms into a second phase. The first phase is assumed to be the oxidic $\alpha\text{-NiMoO}_4$ and the latter one is the sulfided NiMoS_2 . In the following section, this supposition will be re-examined and further elaborated by direct evidence obtained from EXAFS data analysis.

3.2. Catalyst activation and oxysulfide intermediates

We examined the structural evolution of the NiMoPILC catalyst at each stage by carrying out FEFF calculations to analyse the EXAFS experimental data. DFT-generated structural models were also employed for FEFF calculations based on our trial-and-error observation that the bulk structures were not always the appropriate models for NiMoPILC, as they failed to accurately determine the local structure of Mo and Ni atoms. A detailed explanation will be provided below.

Fig. 3(a and b) depict the Fourier transform (FT) magnitude of k^3 -weighted Mo K-edge and Ni K-edge EXAFS (experimental) spectra for stages 1-6. We focus on stages 4-5 since in those stages the major structural changes occurred as previously described in the XANES and ITFA results. The peak profile of the Mo K-edge EXAFS spectra displays a distinct peak transition from 1.26 \AA (oxide) to 1.87 \AA (sulfide) along with an attenuation of its amplitude by half of its maximum value. The oxide-to-sulfide peak transition in the Ni K-edge EXAFS spectra is subtle, exemplified by a less noticeable peak transition from 1.56 \AA (oxide) to 1.69 \AA (sulfide). The oxide-to-sulfide peak transition in the Mo K-edge and Ni K-edge cases presents as

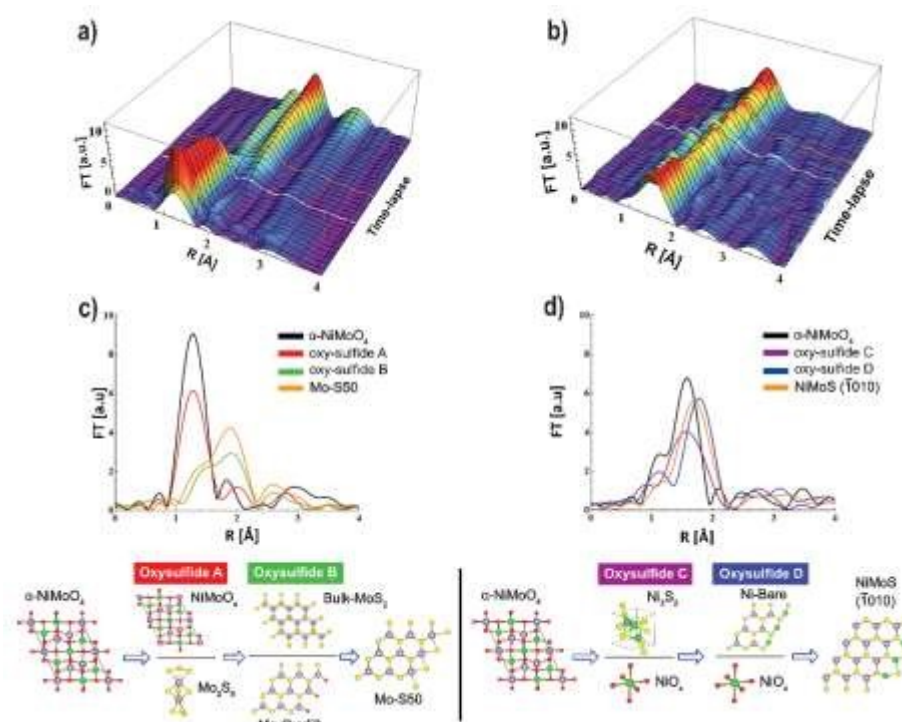


Fig. 3 Fourier transform (FT) magnitude of *in situ* Mo K-edge (a) and Ni K-edge (b) k^3 -weighted EXAFS spectra (with white and orange lines indicate oxysulfides (A,C) and (B,D) positions). Comparison of Mo K-edge (c) and Ni K-edge (d) EXAFS spectra during the sulfidation process (Stages 4-5) and those calculated from the structures shown below. **Bottom:** The proposed oxysulfide structures during the sulfidation process. Purple, green, red, and yellow spheres refer to molybdenum, nickel, oxygen, and sulfur atoms, respectively. **Note:** no phase correction applied.

discontinuous-like and continuous-like peak transitions, respectively. In contrast to the Mo K-edge EXAFS spectra, the broadening of the Ni K-edge EXAFS spectra implies that the local structure of Ni atoms is not well-ordered in both the partially and fully sulfided NiMoPILC catalyst.

In conjunction with the ITFA result, information obtained from the EXAFS spectra could help identify not only the initial and final structures found at stages 4-5, but also possibly reveal the structures of the oxysulfides; the intermediates between the oxidic and the sulfided forms of NiMoPILC. As a starting point, Fig. 3(c and d) outline the FT magnitude Mo K-edge and Ni K-edge EXAFS spectra at stages 4-5. For the sake of clarity, only four EXAFS spectra are presented as representatives of oxide, oxysulfide, and sulfide phases. Detailed information of the Mo K-edge and Ni K-edge EXAFS fitting parameters is tabulated in Tables 1S and 2S (ESI[†]). The EXAFS fitting parameters related to those spectra in Fig. 3(c and d) are given in Tables 1 and 2. From previous EXAFS and XRD studies,^{39,61,62} both Mo and Ni ions in α -NiMoO₄ are reported to occupy the octahedral sites. Our results show that the Mo and Ni atoms located in α -NiMoO₄ have also adopted an octahedral configuration as indicated by the total coordination numbers (CN) of the Mo-O and Ni-O shells which are close to 6. Likewise, the CN of Mo-Mo, Ni-Ni, and Ni-Mo bonds are found to have values of 2, 1.7, and 1.7, respectively. These numbers and also their bond lengths closely match the description of the standard reference α -NiMoO₄. A detailed description of the oxidic α -NiMoO₄ structure has been provided elsewhere.⁶³

While unravelling the α -NiMoO₄ geometry from the Mo K-edge and Ni K-edge EXAFS data is relatively straightforward, more effort is needed to identify the structures of the oxysulfides and NiMoS₂, as their structures are more complex and could not be assigned to known reference materials. In Fig. 3(c), two intermediate EXAFS spectra that lie between the α -NiMoO₄ and Mo-S50 spectra are labelled as oxysulfide A (red line) and oxysulfide B (green line) with their proposed structures shown. Judging from the data given in Table 1, it is proposed that oxysulfide A has a mixed combination of NiMoO_x and Mo₂S₉ as intermediates of suboxide and subsulfide, respectively. At this stage, the degree of molybdenum sulfidation has reached 69% with 31% of oxide remaining as indicated in Fig. 2(c). The coordination number of Mo by oxygen in the NiMoO_x phase has drastically reduced to around two. This indicates that the octahedral sites previously adopted by the Mo atoms in α -NiMoO₄ have broken into an unknown highly dispersed MoO_x structure, which is difficult to identify accurately as reported by Rodriguez *et al.*⁶² Although the coordination numbers are greatly reduced, the bond lengths of Mo-O and Mo-Mo bonds in NiMoO_x and those in α -NiMoO₄ are similar, despite their distinct structural differences. Moreover, the emergence of a short-lived Mo₂S₉ phase (see Fig. 4(a)) could be explained as the result of an S-O exchange reaction⁶⁴ between an octahedral MoO₃-like structure and H₂S gas, that generates water and MoS₂ as by-products.⁶⁵ Supporting evidence for the occurrence

Table 1 Mo K-edge EXAFS fitting parameters of NiMoPILC during the sulfidation process at stages 4-6

Fitting Model	Back scatterer	N	R(Å)	σ^2 (Å ²) x 10 ⁻³	R-factor
Temp 114.4 - 129.1 °C					
α-NiMoO ₄	O	2.4 ± 0.4	1.75 ± 0.04	0.31	0.0146
	O	3.6 ± 0.4	2.26 ± 0.04	18.85	
	Mo	2.0 ± 0.1	3.29 ± 0.01	11.8	
Oxysulfide A					
Temp 379.7 °C					
NiMoO _x	O	1.9 ± 0.2	1.76 ± 0.05	1.13	0.0057
	Mo	1.9 ± 0.2	3.27 ± 0.02	14.75	
Mo ₂ S ₉	S	1.8	2.47 ± 0.05	13.15	
	Mo	0.6	2.77 ± 0.11	11.32	
Oxysulfide B					
Temp 418.8 °C					
Mo-Oxy50	O	0.4	1.72 ± 0.02	3.12	0.0126
Bulk MoS ₂	S	5.9 ± 0.7	2.43 ± 0.01	19.72	
	Mo	5.9 ± 0.7	3.21 ± 0.06	22.43	
	S	5.9 ± 0.7	3.87 ± 0.10	49.15	
Temp 423.6 - 423.7 °C					
Mo-S50	S	5.2 ± 0.7	2.42 ± 0.0	13.74	0.0175
	Mo	3.5 ± 0.5	3.19 ± 0.04	14.05	
	S	1.7 ± 0.2	3.77 ± 0.28	12.29	
Temp 31.6 - 55.4 °C					
Mo-Bare (stage 6)	S	4.4 ± 0.5	2.42 ± 0.06	8.89	0.0194
	Mo	4.4 ± 0.5	3.18 ± 0.11	11.17	
	S	2.2 ± 0.3	3.76 ± 0.13	11.18	
	S	2.2 ± 0.3	4.68 ± 0.05	12.52	
Mo-S50 (stage 6)	S	8.7 ± 1.0	5.28 ± 0.25	25.49	0.0191
	S	4.2 ± 0.5	2.42 ± 0.04	8.88	
	Mo	2.8 ± 0.3	3.18 ± 0.03	8.46	
	S	1.4 ± 0.2	3.73 ± 0.36	10.09	
	S	1.4 ± 0.2	4.70 ± 0.05	8.66	
S	7.0 ± 0.8	5.29 ± 0.23	23.89		

Note: The numbers highlighted in grey indicate the contribution from the Mo₂S₉ phase and bulk MoS₂. Bold numbers correspond to fixed coordination numbers.

of this reaction was observed in the MS data measurement (Fig. 1S, ESI[†]). The Mo-S and Mo-Mo bond distances in Mo₂S₉ from the fitted Mo K-edge EXAFS data are 2.47 Å and 2.77 Å, respectively, which are close to the lengths of Mo-S and Mo-Mo bonds found in the MoS₃ structure.⁶⁶ With this knowledge, the initial assumption was that extending the sulfidation process would definitely convert the MoS₃-like Mo₂S₉ structure (oxysulfide A) into MoS₂ as previously proposed by Weber *et al* in their spectroscopy study.⁶⁷ However, using two atomistic models bulk MoS₂ and Mo-Oxy50 (Fig. 4(b)) as the fitting models for EXAFS data, we found that oxysulfide B still contains a small fraction of MoO_x in the majority MoS₂ phase. This EXAFS data interpretation is also supported by the ITFA calculation, where at that particular time there was 88% sulfided and 12% oxide phases. As illustrated by the model (Fig. 3 bottom part), the outer oxide layer of Mo-Oxy50 is composed of a series of single oxygen atoms where each atom bonded by single Mo edge atom featuring a chain of oxygen decorating the Mo edge surface. Here, the average coordination number of Mo-O shells is almost close to zero which is attributed to near complete sulfidation. The appearance of an Mo-Mo bond contribution at 3.21 Å, which is very close to the Mo-Mo distance of 3.19 Å in

Table 2 Ni K-edge EXAFS fitting parameters of NiMoPILC during the sulfidation process at stages 4-6View Article Online
DOI: 10.1039/D2CP03987G

Fitting Model	Back scatterer	N	R(Å)	σ^2 (Å ²) x 10 ⁻³	R-factor
Temp 127.8 - 159.5 °C					
α-NiMoO ₄	O	5.2 ± 0.5	2.03 ± 0.02	7.56	0.008
	Ni	1.7 ± 0.2	3.02 ± 0.05	19.98	
	Mo	1.7 ± 0.2	3.19 ± 0.05	19.46	
	Mo	1.7 ± 0.2	3.78 ± 0.0	11.94	
Oxysulfide C					
Temp 421.9 °C					
NiO _x	O	5.5	2.05 ± 0.04	14.76	0.0183
Ni ₃ S ₂	S	2	2.16 ± 0.09	12.5	
	Ni	2	2.54 ± 0.04	22.65	
	S	2	3.58 ± 0.09	14.21	
Oxysulfide D					
Temp 425 - 425.2 °C					
NiO _x	O	1	2.01 ± 0.08	7.91	0.0169
Ni-Bare	S	2.4	2.21 ± 0.03	0.74	
	Mo	1.2	2.80 ± 0.05	11.96	
	S	1.2	3.53 ± 0.02	15.60	
Temp 426.1 - 426.6 °C					
NiMoS (1010)	S	2.7 ± 0.4	2.19 ± 0.15	8.16	0.0163
	Mo	0.9 ± 0.1	2.76 ± 0.04	5.34	
	Ni	0.9 ± 0.1	2.94 ± 0.06	6.93	
	S	1.8 ± 0.2	3.52 ± 0.12	8.60	
Temp 29.6 - 40.4 °C					
Ni-Bare (stage 6)	S	2.8 ± 0.4	2.21 ± 0.02	5.5	0.0177
	Mo	1.4 ± 0.2	2.75 ± 0.0	7.36	
	Ni	1.4 ± 0.2	3.12 ± 0.03	7.8	
	S	1.4 ± 0.2	3.51 ± 0.04	0.61	
NiMoS (1010) (stage 6)	S	3.0 ± 0.3	2.22 ± 0.17	5.79	0.0155
	Mo	1.0 ± 0.1	2.76 ± 0.04	2.86	
	Ni	1.0 ± 0.1	2.94 ± 0.06	3.53	
	S	2.0 ± 0.2	3.52 ± 0.13	4.88	

Note: The numbers highlighted in grey indicate the contribution from the Ni₃S₂ phase. Bold numbers correspond to fixed coordination numbers.

the bulk MoS₂ structure, indicates the formation of larger MoS₂ nanolayers. As expected, further sulfidation completes the transformation of Mo-Oxy50 into MoS₂. Further refinement shows that the EXAFS data at the end of sulfidation treatment could be fitted separately by bulk MoS₂ and Mo-S50 (Fig. 4(c)) which give similar CN and bond lengths for Mo-S(1st) contribution (see Table 1S, ESI[†]). While bulk MoS₂ is understandable to represent the structure of basal plane of MoS₂, Mo-S50 reveals the atom arrangement at the Mo-edge in the sulfided NiMoS₂/Al-PILC catalyst. The structural model Mo-S50 closely resembles the proposed stable MoS₂ surface under partial pressure ratio 0.05 < H₂S/H₂ < 10,000 reported by early DFT studies.^{26,27} The only difference is that the sixfold coordinated Mo edge atoms in the latter case possess short (2.8 Å) and long (3.5 Å) Mo-Mo distances while Mo-S50 has only long Mo-Mo distances (3.2 Å).

We found an interesting result at stage 6 when the H₂S/H₂/He gas supply was switched off and He gas was flushed into the reactor cell, creating an inert atmosphere surrounding the catalyst. The Mo edge atoms, which had previously adopted the structure denoted as Mo-S50 (Fig. 4(c)), were found to lose their outermost sulfur atoms, leaving them directly exposed to

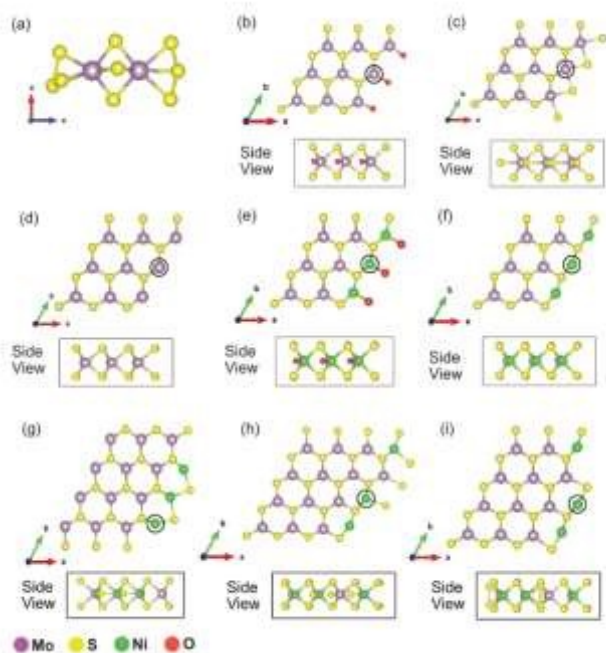


Fig. 4 DFT-calculated Mo and Ni edges that serve as FEFF inputs for EXAFS data fitting analysis. Structural models depicted are denoted as: (a) Mo_2S_2 , (b) Mo-OxyS0, (c) Mo-S50, (d) Mo-Bare, (e) Ni-OxyS0, (f) Ni-Bare, (g) NiMoS ($\bar{1}0\bar{1}0$), (h) NiMoS ($\bar{1}0\bar{1}0$) and (i) NiMoS ($11\bar{2}0$). The last three models are reconstructed based on the proposed models of atom-resolved STM reported in ref. 31 and 32. Purple, green, red, and yellow spheres refer to molybdenum, nickel, oxygen, and sulfur atoms, respectively. Black circle indicates the atom that serves as absorbing (core) atom for EXAFS fitting analysis.

the atmosphere, as depicted in Mo-Bare, Fig. 4(d). The structural model for Mo-Bare has its outer Mo atoms only bonded by four sulfur atoms, rather than six atoms as seen in Mo-S50. A slight reduction of CN in Mo-S(1st) bonds between stage 5 and 6 was confirmed by EXAFS (the fitting parameters are presented in Table 1S, ESI[†]). Using the Hamilton test⁵⁸ performed at similar k - and R -ranges, we found that the EXAFS data at stage 6, when fit with combination of bulk MoS_2 , Mo-S50, and Mo-Bare would always lead to a Mo-S(1st) contribution with a CN value around 4 (see Table 1). This new finding may give explain why the Mo edge atoms on NiMoS₂ in an inert atmosphere are highly reactive as they form coordinatively unsaturated sites (CUS).

Fig. 3(d) also highlights two EXAFS spectra in between the α -NiMoO₄ and NiMoS ($\bar{1}0\bar{1}0$) spectra labelled as oxysulfide C (purple) and oxysulfide D (blue), where their proposed structures are also given. For the Ni-oxysulfides case, we fixed the coordination numbers of both structures since unconstrained values during the EXAFS data fitting tended to give non-physical results. Table 2 reveals that the coordination number of Ni by oxygen in oxysulfide C is still maintained at 5.5, i.e. close to 6. However, this coordination number relates to Ni in the unknown NiO_x phase, not α -NiMoO₄. At this point, the concentration of sulfided and oxide phases has reached 73% and 27%, respectively. Interestingly, the major shell contributions of NiO_x and Ni₃S₂ are dominated by Ni-O, Ni-S, and Ni-Ni bonds. There is no contribution from Ni-Mo backscattering detected. We rationalize the outcome by suggesting that Ni and Mo atoms at that stage have experienced a de-alloying process and then separated into NiS_x and MoS_x

cluster domains. This is consistent with a previous SAXS/XAS study on a CoMoS₂ catalyst,⁶⁸ where a catalyst prepared using a gas phase activation route, was shown to undergo four consecutive stages: (1) oxide, (2) MoS_x domains, (3) aggregation and growth and finally (4) MoS₂ formation. Moreover, as the sulfidation process continued and oxysulfide C transformed into oxysulfide D, the coordination number of Ni by O reduced significantly about 1, in concurrent with the disappearance of Ni₃S₂ phase. The latter structure was replaced by a new phase, Ni-Bare, as depicted in Fig. 4(f). Ni-Bare are similar to NiMoS₂ structures, but with Ni edge atoms not terminated by any sulfur atom. At this stage, the sulfided phase had reached 94% with only 6% remaining oxide. Finally, the extended sulfidation process removed all oxygen from both structures and converted them into NiMoS ($\bar{1}0\bar{1}0$) phase, a NiMoS₂ structure where a small fraction of Ni edge atoms is locally accumulated at particular edge sites and partially terminated by sulfur atoms, as portrayed in Fig. 4(g). In terms of CN and bond lengths, the Ni-S(1st) bonds of NiMoS ($\bar{1}0\bar{1}0$) attain similar physical characteristics to the ones reported in a recent Quick-XAS study of NiMo/Al₂O₃, where the Ni-S(1st) have a bond distance of 2.21 Å and the Ni has a CN between 3.1 - 3.8.⁶⁹ The NiMoS ($\bar{1}0\bar{1}0$) model confirms the presence of a small fraction of Ni edge atoms in NiMoS type B as previously described by STM and STEM.^{31,32} To test this hypothesis, we constructed two other facets of Ni edges of NiMoS type B (see Fig. 4(h) and 4(i)), NiMoS ($10\bar{1}0$) and NiMoS ($11\bar{2}0$) and unsuccessfully attempted to fit them to the EXAFS data. Therefore, the arrangement of Ni edge atoms observed in the sulfided NiMoS₂/Al-PILC catalyst is unique, as the Ni atoms exclusively adopt the NiMoS ($\bar{1}0\bar{1}0$) structure. This implies that the Ni-decorated MoS₂ surface has abundant readily accessible CUS, that makes the surface highly reactive toward oxygenated compounds.

When the catalyst was exposed to an inert atmosphere at stage 6, the NiMoS ($\bar{1}0\bar{1}0$) structure persisted, but a new type of Ni edge site emerges. Based on the EXAFS fit analysis (see Table 2), the geometry of this new Ni edge has zero sulfur coverage as portrayed in Fig. 4(f) and named as Ni-Bare. The structural model of Ni-Bare is similar to that of Mo-Bare structure, in which its outer Ni atoms are only bonded by four sulfur atoms. This suggests that there are two types of Ni edge sites, NiMoS ($\bar{1}0\bar{1}0$) and Ni-Bare, when the catalyst is treated under non-sulfiding gases.

3.3. Guaiacol (GUA) adsorption sites and vibrational frequencies

In the preceding section, we have successfully fit the EXAFS data in the post-sulfidation process (stage 6, see Tables 1 and 2) using four DFT-generated models: Mo-Bare, Mo-S50, Ni-Bare, and NiMoS ($\bar{1}0\bar{1}0$). However, the good fits to the EXAFS data of the models might not guarantee that the exact structures of Mo and Ni at the edges on fresh NiMoS₂/Al-PILC catalyst have been fully revealed. Additional verification can be obtained by calculating the vibrational frequencies of GUA adsorbed on NiMoS₂ and comparing them to available IR and INS spectra. This also answers the unresolved issue of the initial structure of adsorbed GUA on NiMoS₂ prior to decomposition,

hydrodeoxygenation and other reactions. Such work has been done previously on Pt(100) and Pt(111) surfaces⁷⁰, but to the best of our knowledge, no similar endeavour has been conducted for NiMoS₂.

Elaborating which GUA configuration generates a vibrational profile that most closely resembles the INS spectrum is helpful because the INS spectra of free (solid) and adsorbed guaiacol on NiMoS₂ generate almost identical peak profiles (see Fig. 5). This observation indicates that GUA is weakly chemisorbed on NiMoS₂ and hence their adsorption sites are not limited to Mo- and Ni-edge surfaces alone but also might involve the basal plane of MoS₂. The basal plane of MoS₂ might be regarded as an inactive site for HDO processes but a scenario where aromatic compounds such as benzene physisorbed on MoS₂ basal plane via van der Waals interaction has been confirmed by previous DFT studies.^{71,72} Benzene is reported to be preferentially adsorbed in a horizontal (the benzene ring parallel to the basal plane) configuration with an adsorption

of 3.5 Å. The theoretical studies did not consider GUA in their investigation. Test calculation (see Fig. S3, ESI†) shows that benzene adsorbed horizontally on single and bilayer MoS₂ has corresponding adsorption energies of 0.50 and 0.52 eV, in a good agreement with previous DFT studies. GUA adsorbed on bilayer MoS₂ has an adsorption energy of about 0.68 eV i.e. a stronger interaction.

Fig. 6 shows the most stable configurations of GUA adsorbed on the Mo- and Ni-edges found in Mo-Bare, Ni-Bare, Mo-S50, NiMoS ($\bar{1}010$), and the basal plane of MoS₂ in horizontal and vertical configurations, labelled as horiz-basal and vert-basal, respectively. Adsorbed GUA on Mo-Bare and Mo-S50 edge surface has the benzene ring in horizontal (the benzene ring parallel to the edge surface) and vertical configurations, respectively. GUA adsorbed on Ni-Bare and NiMoS ($\bar{1}010$) are in tilted away from the horizontal position at angles of $\sim 32^\circ$ and $\sim 52^\circ$, respectively. The results confirm our previous experimental work that proposed that GUA interacts with

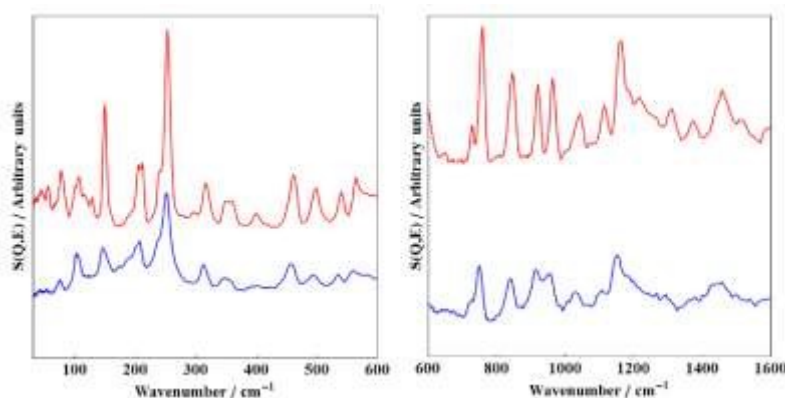


Fig. 5 INS spectra of free guaiacol (red line) and that adsorbed on NiMoS₂/Al-PILC (blue line) at 10 K obtained with TOSCA spectrometer in the energy range 30 - 1600 cm⁻¹. This figure is adapted from ref. 25.

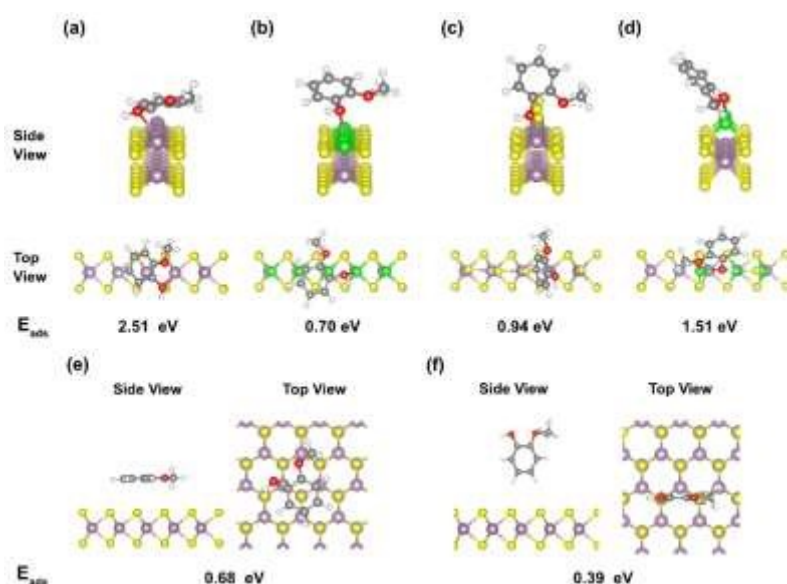


Fig. 6 Most stable configurations of guaiacol adsorbed on (a) Mo-Bare, (b) Ni-Bare, (c) Mo-S50, (d) NiMoS ($\bar{1}010$), (e) horiz-basal and (f) vert-basal with their respective adsorption energy (E_{ads}).

energy range between 0.47 and 0.51 eV at a separation distance NiMoS₂ catalyst mainly through the oxygen atom of the

hydroxyl group,²⁵ in good agreement with a previous DFT study.²⁶ Apart from the edges, GUA is also physisorbed on the MoS₂ basal plane in a horizontal configuration at a separation of about 3.25 Å (see Fig. 6(e)). Under some circumstances, the benzene ring of GUA might orientate itself perpendicular to the basal plane of MoS₂ as portrayed in Fig. 6(f), however, such a configuration is less stable compared to that of horizontally adsorbed GUA. Overall, the bonding strength of guaiacol on the edges and basal plane of NiMoS₂ follows the order: Mo-Bare > NiMoS ($\bar{1}010$) > Mo-S50 > Ni-Bare > planar (basal) > vertical (basal). Chemisorbed GUA is preferentially adsorbed on Mo-Bare rather than NiMoS ($\bar{1}010$) since it attains the highest adsorption energy: 2.51 eV vs 1.51 eV respectively. The result is comparable to the findings reported that on the Pt(100) surface, chemisorbed GUA aligned in a horizontal configuration has adsorption energies between 110 and 241 kJ/mol (1.14-2.5 eV).⁷⁰ Interestingly, this orientation-dependent adsorption has not been observed in previous DFT studies of MoS₂ and CoMoS₂ catalysts.²⁶ This may be because the Mo or Co edges are mostly terminated by sulfur atoms and thus have limited CUS that only allow GUA adsorbed in the horizontal configuration. Additionally, we found that the CUS play a major role in dictating the preferred adsorption sites at the Mo and Ni edges. For instance, NiMoS ($\bar{1}010$) with no available CUS on its Ni edge atoms would interact with GUA exclusively via the S-H bond (not shown) instead of the Ni-O bond as presented in Fig. 6(d). The

S-H bond results in a weaker bonding interaction and has a lower adsorption energy of 0.27 eV. Following the discussion above, the question arises as to whether a higher or lower adsorption energy of GUA would have a direct correlation with its vibrational transition energies.

To provide an answer, a side-by-side comparison between simulated INS spectra of adsorbed GUA on Mo-Bare, Ni-Bare, Mo-S50, NiMoS ($\bar{1}010$), and the MoS₂ basal plane and experimental INS data is presented in Fig. 7. In the energy range between 600 and 1600 cm⁻¹, one could easily observe that the peak patterns of Ni-Bare, Mo-S50, NiMoS ($\bar{1}010$), and MoS₂ basal plane are quite similar and to some extent could fit the experimental INS spectrum notably at 752, 846, 926-963, 1164, and 1463 cm⁻¹. With respect to the INS spectrum of free GUA observed in Fig. 5, these peaks are identified as the ones that remain undisturbed or slightly perturbed when GUA adsorbed on NiMoS₂. This implies that the presence of Mo and Ni edge surfaces along with the basal plane has less profound impact on GUA overall vibrational spectra. This is to be expected because the vibrational modes in this region are mainly those of the benzene ring, which is largely unperturbed on adsorption (see Table S3, ESI[†]). The first and second peaks at 752 and 846 cm⁻¹ correspond to *in-plane* and *out-of-plane* bending of C-H bonds, respectively. The third set of overlapping peaks at 926-963 cm⁻¹ are also due to *out-of-plane* bending in the benzene ring. The fourth peak at 1164 cm⁻¹ can be assigned to in-plane C-H

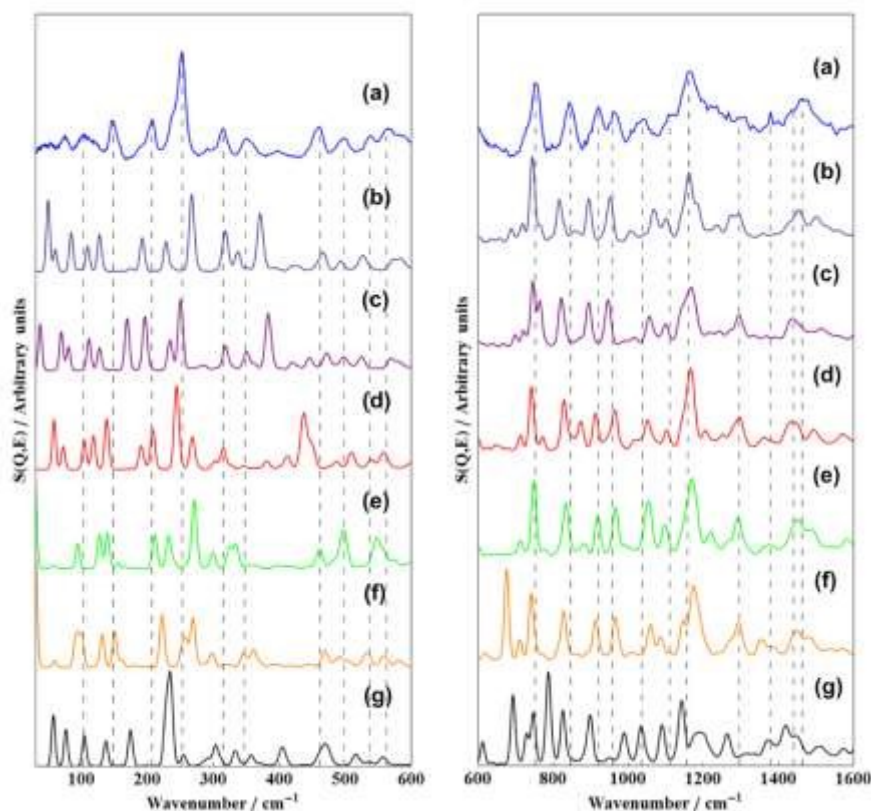


Fig. 7 Comparison of INS spectrum of (a) NiMoS₂/Al-PILC at 10 K dosed with GUA²⁵ and those calculated for GUA adsorbed on (b) vert-basal, (c) horiz-basal, (d) NiMoS ($\bar{1}010$), (e) Ni-Bare, (f) Mo-S50 and (g) Mo-Bare. The vertical dashed lines serve as a guide to the eye. The INS data has the NiMoS₂/Al-PILC contribution subtracted.

bending modes of C-H bonds in the benzene ring. The peak at 1463 cm^{-1} is assigned to a scissoring movement of C-H bonds of the CH_3 group. It is noticeable that the calculated spectrum for GUA on Mo-Bare differs markedly from the INS data and those calculated for the other surfaces. This indicates that chemisorbed GUA on Mo-Bare does not occur in the $\text{NiMoS}_2/\text{Al-PILC}$ catalyst, which suggests that majority of the Mo edge atoms following catalyst activation (or sulfidation process) are fully covered by sulfur atoms. In contrast, the similarity between the INS data and the calculated Ni-Bare spectrum indicates that there are some promoter Ni edge atoms that are not terminated by sulfur atom and hence exposed directly to the air.

In the low energy range between 30 and 600 cm^{-1} , the calculated GUA spectra for each edge surface and the basal plane are comprised of several distinctive peaks that make them distinguishable. This suggests that the vibrational spectra of GUA in the low energy domain is highly sensitive as to which edge, and the orientation on the basal surface, GUA resides on. This is exemplified by the most intense INS peak at 252 cm^{-1} assigned to the CH_3 torsion (methyl torsion) which is observed in both free and adsorbed GUA. The CH_3 torsion of the calculated INS spectra near 252 cm^{-1} are found in GUA adsorbed on $\text{NiMoS}(\bar{1}010)$ and horiz-basal at 243 and 259 cm^{-1} , respectively. The CH_3 torsion mode of GUA on Mo-S50 was found as two bands at 221 and 268 cm^{-1} while it is clearly observed in the Ni-Bare (271 cm^{-1}) and vert-basal (267 cm^{-1}) cases. The vibrational mode observed in Mo-Bare at 254 cm^{-1} corresponds to Mo-O bonds stretching, while its CH_3 torsion mode resides at a lower energy of 234 cm^{-1} . All the band shifting presented above suggests that the methyl torsion of adsorbed GUA is strongly affected by its immediate NiMoS_2 edges and basal plane via intermolecular and/or van der Waals interactions. A similar phenomenon has been observed in methylated unsaturated compounds where the methyl torsion in the unsaturated systems is strongly influenced by its environment.⁷³

Other INS peaks observed at 314 , 346 , and 461 cm^{-1} , which represent out-of-plane deformations (torsions) of the benzene ring, can be found in adsorbed GUA on the MoS_2 basal plane for both the horizontal and vertical benzene ring configurations. Contributions from the Mo and Ni edges could only fit one of the three INS peaks described above. The calculated INS spectra for vert-basal, horiz-basal, and $\text{NiMoS}(\bar{1}010)$ cases at 346 - 461 cm^{-1} generate an artificial single band assigned to the bending mode of C-OH since no observation found in the INS data of both free and adsorbed GUA. In addition, low energy bands between 100 and 250 cm^{-1} in the INS data are characterized by the *out-of-plane* benzene ring deformation and a scissoring movement of the C-O bonds of the hydroxyl and methoxy groups modes at 147 and 206 cm^{-1} , respectively. These two INS peaks are unequivocally observed in all the calculated spectra but their intensity varies greatly and strongly depends on the atomic configurations at the Mo and Ni edges and MoS_2 basal plane. The bands at less than 100 cm^{-1} are generally dominated by translational and rotational modes of adsorbed GUA.²⁵

In summary, based on the differences observed in the calculated vibrational spectrum of GUA for each edge surface and basal plane, we propose that GUA interacts with the edges of NiMoS_2 catalyst mainly through the oxygen atom of the hydroxyl group with its benzene ring being oriented in a tilted configuration on Ni-Bare and $\text{NiMoS}(\bar{1}010)$ edge surfaces, but prefers a vertical (perpendicular) configuration on the Mo-S50 edge surface. Despite being the most stable configuration, GUA has a low probability to be adsorbed on Mo-Bare as demonstrated by its spectral profile at 30 - 1600 cm^{-1} which diverges from that of the INS data. This implies a large share of the Mo-edge surface is fully terminated by sulfur atoms. Based on the similarity between the observed and calculated INS spectra, physisorbed GUA on the MoS_2 basal plane is undoubtedly present. Overall, the spectra strongly suggest that GUA is adsorbed at both the edges and the basal planes of NiMoS_2 .

Conclusions

Intermediate structures (oxysulfides) of $\text{NiMoS}_2/\text{Al-PILC}$ during catalyst activation process have been elaborated using *in situ* XAFS in conjunction with DFT calculations. At an early stage of the sulfidation process, the $\alpha\text{-NiMoO}_4$ structure of oxidic NiMoPILC is transformed into a mixture of ill-defined suboxides (MoO_x , NiO_x) and well-known subsulfides (Mo_2S_9 , Ni_3S_2). These then reconstruct into MoS_2 with two distinctive edges, oxygen-decorated Mo and Ni with no sulfur coverage, that at a later stage, evolves into the sulfided NiMoS_2 catalyst. The Mo and Ni edges of the freshly sulfided catalyst mainly consist of Mo-S50 and a disordered structure of $\text{NiMoS}(\bar{1}010)$ after exposure to sulfiding agents. The existence of $\text{NiMoS}(\bar{1}010)$ facets suggests that NiMoS_2 supported on Al-PILC falls into the NiMoS type B category. The EXAFS fitting analysis indicates that Mo-S50 and $\text{NiMoS}(\bar{1}010)$ facets partially evolve into Mo-Bare and Ni-Bare when the sulfiding gasses are replaced by an inert atmosphere. Using a previous inelastic neutron scattering study as a reference system, DFT calculations of GUA adsorption and its vibrational spectrum reveals that the structural edges of fresh NiMoS_2 catalyst are predominantly characterized by Mo-S50, Ni-Bare, $\text{NiMoS}(\bar{1}010)$ edges as well as the MoS_2 basal plane. The results confirm that GUA weakly interacts with the NiMoS_2 catalyst through: 1) the oxygen atom of the hydroxyl group with two different benzene ring orientations: tilted-up on Ni-edge surfaces and vertically on Mo-edge surfaces; and 2) a van der Waals interaction with the benzene ring parallel to the surface of MoS_2 basal plane.

Conflicts of interest

There are no conflicts to declare.

Acknowledgements

The UK-Indonesia Science and Technology Partnership on STEM Skills for Large Facilities, supported by the Newton Fund and

delivered by STFC ISIS, Diamond, and LIPI is gratefully thanked for financial support of this project. Diamond Light Source Ltd is thanked for access to B18 beamline (SW22907) and the ISIS Neutron and Muon Source for beamtime (RB1810048⁷⁴). The numerical calculations presented here were done using the computing resources provided by STFC Scientific Computing Department's SCARF cluster and Mahameru – BRIN HPC. The authors also acknowledge Diego Gianolio, James Bucag, and Wahyu Bambang Widayatno for their support and assistance during the *in situ* XAFS measurements. One of the authors (WTC) would like to thank DRPM for WCR-scheme of 2021.

Notes and references

- 1 S. K. Hoekman, A. Broch, C. Robbins, E. Ceniceros and M. Natarajan, *Renew. Sustain. Energy Rev.*, 2012, **16**, 143–169.
- 2 J. K. Saini, R. Saini and L. Tewari, *3 Biotech*, 2015, **5**, 337–353.
- 3 S. N. Naik, V. V. Goud, P. K. Rout and A. K. Dalai, *Renew. Sustain. Energy Rev.*, 2010, **14**, 578–597.
- 4 D. A. Ruddy, J. A. Schaidle, J. R. Ferrell III, J. Wang, L. Moens and J. E. Hensley, *Green Chem.*, 2014, **16**, 454–490.
- 5 I. D. Mora-vergara, L. H. Moscoso, E. M. Gaigneaux, S. A. Giraldo and V. G. Baldovino-Medrano, *Catal. Today*, 2018, **302**, 125–135.
- 6 Y.-C. Lin, C.-L. Li, H.-P. Wan, H.-T. Lee and C. Liu, *Energy Fuels*, 2011, **25**, 890–896.
- 7 B. Güvenatam, O. Kurşun, E. H. J. Heeres, E. A. Pidko and E. J. M. Hensen, *Catal. Today*, 2014, **233**, 83–91.
- 8 S. Jin, Z. Xiao, C. Li, X. Chen, L. Wang, J. Xing, W. Li and C. Liang, *Catal. Today*, 2014, **234**, 125–132.
- 9 R. N. Olcese, J. Francois, M. M. Bettahar, D. Petitjean and A. Dufour, *Energy and Fuels*, 2013, **27**, 975–984.
- 10 K. L. Deutsch and B. H. Shanks, *Appl. Catal. A Gen.*, 2012, **447–448**, 144–150.
- 11 E. Laurent, A. Centeno and B. Delmon, *Stud. Surf. Sci. Catal.*, 1994, **88**, 573–578.
- 12 E. Furimsky and F. E. Massoth, *Catal. Today*, 1999, **52**, 381–495.
- 13 E. Laurent and B. Delmon, *J. Catal.*, 1994, **146**, 281–291.
- 14 G. M. Bremmer, L. Van Haandel, E. J. M. Hensen, J. W. M. Frenken and P. J. Kooyman, *J. Phys. Chem. B*, 2016, **120**, 19204–19211.
- 15 P. Afanasiev and C. Lorentz, *J. Phys. Chem. C*, 2019, **123**, 7486–7494.
- 16 F. P. Bouxin, X. Zhang, I. N. Kings, A. F. Lee, M. J. H. Simmons, K. Wilson and S. D. Jackson, *Appl. Catal. A Gen.*, 2017, **539**, 29–37.
- 17 A. Srifa, N. Viriya-Empikul, S. Assabumrungrat and K. Faungnawakij, *Catal. Sci. Technol.*, 2015, **5**, 3693–3705.
- 18 D. Kubička and J. Horáček, *Appl. Catal. A Gen.*, 2011, **394**, 9–17.
- 19 P. M. Mortensen, D. Gardini, C. D. Damsgaard, J. D. Grunwaldt, P. A. Jensen, J. B. Wagner and A. D. Jensen, *Appl. Catal. A Gen.*, 2016, **523**, 159–170.
- 20 S. Mahamulkar, K. Yin, P. K. Agrawal, R. J. Davis, C. W. Jones, A. Malek and H. Shibata, *Ind. Eng. Chem. Res.*, 2016, **55**, 9760–9818.
- 21 A. Popov, E. Kondratieva, J. M. Goupil, L. Mariey, P. Bazin, J. Gilson, A. Travert and F. Mauge, *J. Phys. Chem. C*, 2010, **114**, 15661–15670.
- 22 A. Popov, E. Kondratieva, L. Mariey, J. M. Goupil, J. El Fallah, J. Gilson, A. Travert and F. Mauge, *J. Catal.*, 2013, **297**, 176–186.
- 23 S. Ben Chaabene, L. Bergaoui, A. Ghorbel, J. F. Lambert and P. Grange, *Appl. Catal. A Gen.*, 2004, **268**, 25–31.
- 24 S. A. Zubkov, L. M. Kustov, V. B. Kazansky, G. Fetter, D. Tichit and F. Figueras, *Clays Clay Miner.*, 1994, **42**, 421–427.
- 25 I. B. Adilina, N. Rinaldi, S. P. Simanungkalit, F. Aulia, F. Oemry, G. B. G. Stenning, I. P. Silverwood and S. F. Parker, *J. Phys. Chem. C*, 2019, **123**, 21429–21439.
- 26 M. Badawi, J. Paul, S. Cristol and Payen, *Catal. Commun.*, 2011, **12**, 901–905.
- 27 M. Badawi, S. Cristol, J. F. Paul and E. Payen, *Comptes Rendus Chim.*, 2009, **12**, 754–761.
- 28 M. Badawi, J.-F. Paul, E. Payen, Y. Romero, F. Richard, S. Brunet, A. Popov, E. Kondratieva, J. Gilson, L. Mariey, A. Travert and F. Mauge, *Oil Gas Sci. Technol.*, 2013, **68**, 829–840.
- 29 X. Liu, Q. Wei, W. Huang, Y. Zhou, P. Zhang and Z. Xu, *Fuel*, 2020, **280**, 118669.
- 30 J. V. Lauritsen, M. V. Bollinger, E. Lægsgaard, K. W. Jacobsen, J. K. Nørskov and B. S. Clausen, *J. Catal.*, 2004, **221**, 510–522.
- 31 J. V. Lauritsen, J. Kibsgaard, G. H. Olesen, P. G. Moses, B. Hinnemann, S. Helveg, J. K. Nørskov, B. S. Clausen, H. Topsøe, E. Lægsgaard and F. Besenbacher, *J. Catal.*, 2007, **249**, 220–233.
- 32 F. Besenbacher, M. Brorson, B. S. Clausen, S. Helveg, B. Hinnemann, J. Kibsgaard, J. V. Lauritsen, P. G. Moses, J. K. Nørskov and H. Topsøe, *Catal. Today*, 2008, **130**, 86–96.
- 33 S. Helveg, J. V. Lauritsen, E. Lægsgaard, I. Stensgaard, J. K. Nørskov, B. S. Clausen, H. Topsøe and F. Besenbacher, *Phys. Rev. Lett.*, 2000, **84**, 951–954.
- 34 Y. Zhu, Q. M. Ramasse, M. Brorson, P. G. Moses, L. P. Hansen, C. F. Kisielowski and S. Helveg, *Angew. Chemie Int. Ed.*, 2014, **53**, 10723–10727.
- 35 Y. Zhu, Q. M. Ramasse, M. Brorson, P. G. Moses, L. P. Hansen, H. Topsøe, C. F. Kisielowski and S. Helveg, *Catal. Today*, 2016, **261**, 75–81.
- 36 D. Ferdous, A. K. Dalai and J. Adjaye, *J. Mol. Catal. A Chem.*, 2005, **234**, 169–179.
- 37 R. G. Leliveld, A. J. Van Dillen, J. W. Geus and D. C. Koningsberger, *J. Catal.*, 1997, **171**, 115–129.
- 38 Y. Hamabe, S. Jung, H. Suzuki, N. Koizumi and M. Yamada, *J. Synchrotron Radiat.*, 2010, **17**, 530–539.
- 39 A. Rochet, B. Baubet, V. Moizan, E. Devers, A. Hugon, C. Pichon, E. Payen and V. Briois, *J. Phys. Chem. B*, 2015, **119**, 23928–23942.
- 40 A. Rochet, B. Baubet, V. Moizan, E. Devers, A. Hugon, C. Pichon, E. Payen and V. Briois, *J. Phys. Chem. C*, 2017, **121**, 18544–18556.
- 41 T. Shido and R. Prins, *J. Phys. Chem. B*, 1998, **102**, 8426–8435.

- 42 G. Plazenet, S. Cristol, J. F. Paul, E. Payen and J. Lynch, *Phys. Chem. Chem. Phys.*, 2001, **3**, 246–251.
- 43 A. J. Dent, G. Cibir, S. Ramos, A. D. Smith, S. M. Scott, L. Varandas, M. R. Pearson, N. A. Krumpa, C. P. Jones and P. E. Robbins, *J. Phys. Conf. Ser.*, 2009, **190**, 012039.
- 44 A. B. Kroner, K. M. H. Mohammed, M. Gilbert, G. Duller, L. Cahill, P. Leicester, R. Woolliscroft and E. J. Shotton, *AIP Conf. Proc.*, 2016, **1741**, 030014.
- 45 B. Ravel and M. Newville, *J. Synchrotron Radiat.*, 2005, **12**, 537–541.
- 46 ICSD FIZ Karlsruhe, <https://icsd.products.fiz-karlsruhe.de/>.
- 47 W. Rasband, ImageJ, <https://imagej.nih.gov/ij/>.
- 48 G. Kresse and J. Furthmüller, *Phys. Rev. B. Condens. Matter*, 1996, **54**, 11169–11186.
- 49 G. Kresse, *Comput. Mater. Sci.*, 1996, **6**, 15–50.
- 50 Y. Wang and J. P. Perdew, *Phys. Rev. B*, 1991, **44**, 13298–13307.
- 51 J. P. Perdew and Y. Wang, *Phys. Rev. B*, 1992, **45**, 13244–13249.
- 52 G. Kresse and D. Joubert, *Phys. Rev. B - Condens. Matter Mater. Phys.*, 1999, **59**, 1758–1775.
- 53 H. J. Monkhorst and J. D. Pack, *Phys. Rev. B*, 1976, **13**, 5188–5192.
- 54 Chemcraft - graphical software for visualization of quantum chemistry computations, <https://www.chemcraftprog.com>.
- 55 K. Dymkowski, S. F. Parker, F. Fernandez-Alonso and S. Mukhopadhyay, *Phys. B Condens. Matter*, 2018, **551**, 443–448.
- 56 O. Arnold, J. C. Bilheux, J. M. Borreguero, A. Buts, S. I. Campbell, L. Chapon, M. Doucet, N. Draper, R. Ferraz Leal, M. A. Gigg, V. E. Lynch, A. Markvardsen, D. J. Mikkelsen, R. L. Mikkelsen, R. Miller, K. Palmen, P. Parker, G. Passos, T. G. Perring, P. F. Peterson, S. Ren, M. A. Reuter, A. T. Savici, J. W. Taylor, R. J. Taylor, R. Tolchenov, W. Zhou and J. Zikovsky, *Nucl. Instruments Methods Phys. Res. Sect. A*, 2014, **764**, 156–166.
- 57 S. Eijbsbouts, L. C. A. Van Den Oetelaar and R. R. Van Puijenbroek, *J. Catal.*, 2005, **229**, 352–364.
- 58 S. Calvin, *XAFS for Everyone*, CRC Press, New York, 1st editio., 2013.
- 59 A. Rossberg, T. Reich and G. Bernhard, *Anal. Bioanal. Chem.*, 2003, **376**, 631–638.
- 60 A. Rossberg, K. U. Ulrich, S. Weiss, S. Tsushima, T. Hiemstra and A. C. Scheinost, *Environ. Sci. Technol.*, 2009, **43**, 1400–1406.
- 61 R. Cattaneo, T. Weber, T. Shido and R. Prins, *J. Catal.*, 2000, **191**, 225–236.
- 62 J. A. Rodriguez, J. Y. Kim and J. C. Hanson, *Catal. Letters*, 2002, **82**, 103–109.
- 63 J. A. Rodriguez, J. C. Hanson, S. Chaturvedi, A. Maiti and J. L. Brito, , DOI:10.1063/1.480619.
- 64 T. Weber, J. C. Muijsers, J. H. M. C. Van Wolput, C. P. J. Verhagen and J. W. Niemantsverdriet, *J. Phys. Chem.*, 1996, **100**, 14144–14150.
- 65 P. Arnoldy, J. A. M. van den Heijkant, G. D. de Bok and J. A. Moulun, *J. Catal.*, 1985, **55**, 35–55.
- 66 S. J. Hibble, D. A. Rice, D. M. Pickup and M. P. Beier, *Inorg. Chem.*, 1995, **34**, 5109–5113. DOI: 10.1039/D2CP03987G
- 67 T. Weber, J. C. Muijsers and J. W. Niemantsverdriet, *J. Phys. Chem.*, 1995, **99**, 9194–9200.
- 68 L. van Haandel, A. Longo, W. Bras, E. J. M. Hensen and T. Weber, *ChemCatChem*, 2019, **11**, 5013–5017.
- 69 A. Rochet, B. Baubet, V. Moizan, E. Devers, A. Hugon, C. Pichon, E. Payen and V. Briois, *J. Phys. Chem. C*, 2015, **119**, 23928–23942.
- 70 E. V. Scoullios, M. S. Hofman, Y. Zheng, D. V. Potapenko, Z. Tang, S. G. Podkolzin and B. E. Koel, *J. Phys. Chem. C*, 2018, **122**, 29180–29189.
- 71 P. G. Moses, J. J. Mortensen, B. I. Lundqvist and J. K. Nørskov, *J. Chem. Phys.*, 2009, **130**, 104709.
- 72 L. N. Pham and T. R. Walsh, *Chem. Sci.*, 2022, 5186–5195.
- 73 A. Zachariou, A. P. Hawkins, P. Collier, R. F. Howe, D. Lennon and S. F. Parker, *ACS Omega*, 2020, **5**, 2755–2765.
- 74 I. B. Adilina, N. Rinaldi, S. F. Parker, F. Oemry, F. Aulia and S. P. Simanungkalit, Catalytic Hydrodeoxygenation of a Lignin Model Compound - TOSCA, <https://data.isis.stfc.ac.uk/doi/STUDY/103195270/>.

**Electronic Supplementary Information for:
“Experimental and Computational Studies of Sulfided NiMo/Al-PILC:
Catalyst Activation and Guaiacol Adsorption Sites”**

F. Oemry,^{*a} I. B. Adilina,^b W. T. Cahyanto,^c N. Rinaldi,^b F. Aulia,^b A. Jackson,^d S. F. Parker,^e
A. B. Kroner,^f E. J. Shotton^f

^aResearch Center for Quantum Physics, National Research and Innovation Agency, Kawasan Puspiptek Serpong, Tangerang Selatan, Banten 15314, Indonesia

Email: fere001@brin.go.id

^bResearch Center for Advanced Chemistry, National Research and Innovation Agency, Kawasan Puspiptek Serpong, Tangerang Selatan, Banten 15314, Indonesia

^cDepartment of Physics, Universitas Jenderal Soedirman, Jl. dr. Soeparno 61, Purwokerto 53122, Indonesia

^dScientific Computing Department, STFC Rutherford Appleton Laboratory, Chilton, Didcot, Oxfordshire OX11 0QX, United Kingdom

^eISIS Neutron and Muon Source, STFC Rutherford Appleton Laboratory, Chilton, Didcot, Oxfordshire OX11 0QX, United Kingdom

^fDiamond Light Source Ltd, Diamond House, Harwell Science and Innovation Campus, Didcot, Oxfordshire, OX11 0DE, United Kingdom

Table 1S: Mo K-edge EXAFS fitting parameters of NiMoPILC (*in situ*)

No.	Fitting model	Back scatterer	N	R(Å)	σ^2 (Å ²) x 10 ⁻³	R-factor	Time-lapse	temp in °C
Stage 4 ($\Delta k = 3 - 11 \text{ \AA}^{-1}$, H₂S/H₂/He gasses)								
1	NiMoO ₄	O	2.4 ± 0.4	1.75 ± 0.04	0.31	0.0146	0:24:34	114.4 - 129.1
		O	3.6 ± 0.4	2.26 ± 0.04	18.85			
		Mo	2.0 ± 0.1	3.29 ± 0.01	11.8			
2	NiMoO ₄	O	2.9 ± 0.4	1.75 ± 0.04	1.44	0.0123	0:27:38	147 - 164.6
		O	3.1 ± 0.4	2.25 ± 0.05	19.79			
		Mo	2.0 ± 0.1	3.28 ± 0.01	13.85			
3	NiMoO ₄	O	2.8 ± 0.4	1.75 ± 0.04	1.27	0.0118	0:30:43	182.9 - 201.2
		O	3.2 ± 0.4	2.25 ± 0.05	19.69			
		Mo	2.0 ± 0.1	3.28 ± 0.01	14.09			
4	NiMoO ₄	O	2.8 ± 0.4	1.75 ± 0.04	1.41	0.0111	0:33:47	219.6 - 237.8
		O	3.2 ± 0.4	2.24 ± 0.06	19.8			
		Mo	2.0 ± 0.1	3.28 ± 0.02	14.44			
5	NiMoO ₄	O	2.7 ± 0.4	1.75 ± 0.04	1.56	0.0108	0:38:23	256.2 - 293.1
		O	3.3 ± 0.4	2.23 ± 0.07	19.54			
		Mo	2.0 ± 0.1	3.27 ± 0.02	15.1			
6	NiMoO ₄	O	2.8 ± 0.4	1.75 ± 0.04	1.98	0.0105	0:39:55	308.8
		O	3.2 ± 0.4	2.22 ± 0.08	19.5			
		Mo	2.0 ± 0.1	3.27 ± 0.03	15.81			
7	NiMoO ₄	O	2.9 ± 0.4	1.75 ± 0.04	2.27	0.0102	0:41:27	328.2
		O	3.2 ± 0.4	2.2 ± 0.09	19.21			
		Mo	2.0 ± 0.1	3.26 ± 0.03	16.2			
8	NiMoO ₄	O	2.9 ± 0.3	1.75 ± 0.04	2.74	0.0115	0:43:00	345.9
		O	3.1 ± 0.3	2.18 ± 0.12	17.17			
		Mo	2.0 ± 0.1	3.25 ± 0.05	17.33			
9	NiMoO ₄	O	2.9 ± 0.5	1.75 ± 0.04	3.65	0.0198	0:44:32	363.7
		O	3.2 ± 0.5	2.15 ± 0.15	14.29			
		Mo	2.0 ± 0.2	3.22 ± 0.07	17.85			
10	NiMoO ₄	O	1.9 ± 0.2	1.76 ± 0.05	1.13	0.0057	0:46:04	379.7
		Mo	1.9 ± 0.2	3.27 ± 0.02	14.75			
	Mo ₂ S ₉	S	1.8	2.47 ± 0.05	13.15			
	Mo	0.6	2.77 ± 0.11	11.32				
11	NiMoO ₄	O	1.5 ± 0.1	1.76 ± 0.04	0.39	0.0060	0:47:36	396.3
		Mo	1.5 ± 0.1	3.25 ± 0.04	12.93			
	Mo ₂ S ₉	S	1.6	2.45 ± 0.03	10.07			
	Mo	0.5	2.74 ± 0.08	10.77				
Stage 5 ($\Delta k = 3 - 11 \text{ \AA}^{-1}$, H₂S/H₂/He gasses)								
12	NiMoO ₄	O	0.9 ± 0.3	1.75 ± 0.04	1.81	0.0209	0:56:49	418.1
		Mo	0.9 ± 0.3	3.22 ± 0.07	9.74			
		Mo ₂ S ₉	S	2.9 ± 0.7	2.44 ± 0.03			
13	NiMoO ₄	O	0.6 ± 0.3	1.74 ± 0.03	0.87	0.0204	0:58:21	420
		Mo	0.6 ± 0.3	3.20 ± 0.09	7.10			
		Mo ₂ S ₉	S	3.2 ± 0.9	2.43 ± 0.02			
14	Mo-Oxy50	O	0.4	1.74 ± 0.05	0.32	0.0233	0:59:53	422.1
		S	3.5 ± 0.6	2.44 ± 0.04	15.22			
		Mo	3.5 ± 0.6	3.24 ± 0.01	19.79			
		S	1.8 ± 0.3	3.82 ± 0.23	13.37			

... continued

15	Mo-Oxy50	O	0.3	1.72 ± 0.03	1.0	0.0218	1:01:25	423.7	
		S	4.0 ± 0.7	2.43 ± 0.03	15.77				
		Mo	4.0 ± 0.7	3.23 ± 0.02	20.0				
		S	2.0 ± 0.4	3.81 ± 0.24	14.12				
16	Mo-Oxy50 Bulk MoS ₂	O	0.4	1.73 ± 0.04	1.78	0.0125	1:02:57	423.5	
		S	5.7 ± 0.7	2.44 ± 0.03	20.04				
		Mo	5.7 ± 0.7	3.23 ± 0.08	21.46				
		S	5.7 ± 0.7	3.86 ± 0.11	25.10				
17	Mo-Oxy50 Bulk MoS ₂	O	0.4	1.72 ± 0.02	3.12	0.0126	1:04:29	418.8	
		S	5.9 ± 0.7	2.43 ± 0.01	19.72				
		Mo	5.9 ± 0.7	3.21 ± 0.06	22.43				
		S	5.9 ± 0.7	3.87 ± 0.10	49.15				
18	Mo-Oxy50 Bulk MoS ₂	O	0.5	1.71 ± 0.02	6.47	0.0150	1:06:01	418.1	
		S	6.6 ± 0.9	2.43 ± 0.02	20.46				
		Mo	6.6 ± 0.9	3.22 ± 0.07	21.95				
		S	6.6 ± 0.9	3.85 ± 0.12	26.59				
19	Mo-Oxy50 Bulk MoS ₂	O	0.5	1.71 ± 0.01	7.72	0.0161	1:07:34	420	
		S	6.6 ± 0.9	2.43 ± 0.02	20.08				
		Mo	6.6 ± 0.9	3.21 ± 0.06	21.83				
		S	6.6 ± 0.9	3.85 ± 0.12	26.69				
20	Mo-Oxy50 Bulk MoS ₂	O	0.4	1.69 ± 0.0	5.97	0.0125	1:09:06	419.3	
		S	6.4 ± 0.8	2.43 ± 0.01	19.16				
		Mo	6.4 ± 0.8	3.21 ± 0.06	21.48				
		S	6.4 ± 0.8	3.84 ± 0.12	26.34				
21	Bulk MoS ₂	$(\Delta k = 3 - 10 \text{ \AA}^{-1}, \text{H}_2\text{S}/\text{H}_2/\text{He gasses})$					0.0224	1:13:42	420.5 - 421.6
		S	5.4 ± 0.9	2.42 ± 0.0	15.78				
		Mo	5.4 ± 0.9	3.20 ± 0.05	18.91				
		S	5.4 ± 0.9	3.81 ± 0.15	24.53				
22	Bulk MoS ₂	S	5.3 ± 0.8	2.42 ± 0.0	15.14	0.0201	1:18:19	421.5 - 422.5	
		Mo	5.3 ± 0.8	3.19 ± 0.04	18.69				
		S	5.3 ± 0.8	3.82 ± 0.15	24.41				
		S	5.3 ± 0.8	2.42 ± 0.0	15.14				
23	Bulk MoS ₂	Mo	5.3 ± 0.8	3.19 ± 0.04	18.69	0.0201	1:21:23	420.4 - 421.9	
		S	5.3 ± 0.8	3.82 ± 0.15	24.41				
		S	5.5 ± 0.8	2.42 ± 0.0	15.15				
		Mo	5.5 ± 0.8	3.19 ± 0.04	18.28				
24	Bulk MoS ₂	S	5.5 ± 0.8	3.81 ± 0.16	24.54	0.0196	1:27:31	420.8 - 423.3	
		Mo	5.5 ± 0.8	3.19 ± 0.04	18.28				
		S	5.5 ± 0.8	3.81 ± 0.16	24.54				
		S	5.5 ± 0.8	2.42 ± 0.0	15.15				
25	Bulk MoS ₂	$(\Delta k = 3 - 10.2 \text{ \AA}^{-1}, \text{H}_2\text{S}/\text{H}_2/\text{He gasses})$					0.0202	1:35:12	419.6 - 423.4
		S	5.3 ± 0.8	2.42 ± 0.0	14.34				
		Mo	5.3 ± 0.8	3.19 ± 0.04	17.81				
	Mo-S50	S	5.3 ± 0.8	3.81 ± 0.16	24.20	0.0192			
		S	5.2 ± 0.7	2.42 ± 0.0	14.44				
		Mo	3.5 ± 0.5	3.19 ± 0.04	14.74				
		S	1.7 ± 0.2	3.77 ± 0.28	12.26				
26	Bulk MoS ₂	S	5.3 ± 0.7	2.42 ± 0.0	13.76	0.0197	1:45:57	419.9 - 423.7	
		Mo	5.3 ± 0.7	3.19 ± 0.04	17.40				
		S	5.3 ± 0.7	3.81 ± 0.16	24.33				
	Mo-S50	S	5.2 ± 0.7	2.42 ± 0.0	13.86	0.0187			
		Mo	3.5 ± 0.5	3.19 ± 0.04	14.35				
		S	1.7 ± 0.2	3.78 ± 0.27	12.63				

... continued

27	Bulk MoS ₂	S	5.3 ± 0.7	2.42 ± 0.0	13.61	0.0187	1:49:01	423.6 - 423.7		
		Mo	5.3 ± 0.7	3.19 ± 0.04	17.12					
		S	5.3 ± 0.7	3.81 ± 0.16	24.21					
	Mo-S50	S	5.2 ± 0.7	2.42 ± 0.0	13.74	0.0175				
		Mo	3.5 ± 0.5	3.19 ± 0.04	14.05					
		S	1.7 ± 0.2	3.77 ± 0.28	12.29					
Stage 6 ($\Delta k = 3.2 - 11 \text{ \AA}^{-1}$, He gas)										
28	Mo-Bare	S	4.5 ± 0.5	2.41 ± 0.05	11.71	0.0173	1:58:14	345.2 - 422		
		Mo	4.5 ± 0.5	3.19 ± 0.04	15.53					
		S	2.5 ± 0.3	3.77 ± 0.13	13.17					
		S	2.5 ± 0.3	4.61 ± 0.02	16.40					
		S	10.0 ± 1.0	5.32 ± 0.29	28.50					
	Mo-S50	S	4.2 ± 0.5	2.41 ± 0.03	11.58	0.0178				
		Mo	2.8 ± 0.3	3.18 ± 0.03	12.53					
		S	1.4 ± 0.2	3.75 ± 0.30	11.54					
		S	1.4 ± 0.2	4.64 ± 0.01	12.82					
		S	7.0 ± 0.8	5.34 ± 0.27	26.78					
29	Mo-Bare	S	4.3 ± 0.5	2.41 ± 0.05	10.80	0.0182	2:07:27	238.4 - 325.4		
		Mo	4.3 ± 0.5	3.17 ± 0.04	14.22					
		S	2.2 ± 0.2	3.77 ± 0.13	12.10					
		S	2.2 ± 0.2	4.63 ± 0.0	15.74					
		S	8.7 ± 0.9	5.32 ± 0.29	27.97					
	Mo-S50	S	4.1 ± 0.4	2.41 ± 0.03	10.70	0.0186				
		Mo	2.7 ± 0.3	3.18 ± 0.03	11.31					
		S	1.4 ± 0.1	3.75 ± 0.30	10.73					
		S	1.4 ± 0.1	4.66 ± 0.01	11.51					
		S	6.8 ± 0.7	5.33 ± 0.27	26.54					
30	Mo-Bare	S	4.3 ± 0.5	2.42 ± 0.05	9.85	0.0189	2:15:08	172.3 - 224		
		Mo	4.3 ± 0.5	3.18 ± 0.12	12.96					
		S	2.1 ± 0.2	3.77 ± 0.13	11.65					
		S	2.1 ± 0.2	4.64 ± 0.01	14.49					
		S	8.5 ± 0.9	5.32 ± 0.29	27.47					
	Mo-S50	S	4.0 ± 0.4	2.41 ± 0.03	9.76	0.0194				
		Mo	2.7 ± 0.3	3.18 ± 0.03	10.11					
		S	1.3 ± 0.1	3.74 ± 0.31	10.22					
		S	1.3 ± 0.1	4.67 ± 0.02	10.28					
		S	6.7 ± 0.7	5.33 ± 0.26	25.99					
($\Delta k = 3.3 - 11 \text{ \AA}^{-1}$, He gas)										
31	Mo-Bare	S	4.3 ± 0.5	2.42 ± 0.05	9.53	0.0188	2:24:20	116.4 - 160.9		
		Mo	4.3 ± 0.5	3.18 ± 0.11	12.30					
		S	2.2 ± 0.2	3.77 ± 0.13	11.56					
		S	2.2 ± 0.2	4.66 ± 0.03	14.63					
		S	8.6 ± 1.0	5.30 ± 0.27	26.80					
	($\Delta k = 3.2 - 11 \text{ \AA}^{-1}$, He gas)									
	Mo-S50	S	4.0 ± 0.5	2.41 ± 0.03	9.25	0.0209				
		Mo	2.7 ± 0.3	3.18 ± 0.03	9.38					
		S	1.3 ± 0.1	3.74 ± 0.31	10.03					
		S	1.3 ± 0.1	4.68 ± 0.03	9.39					
S		6.7 ± 0.8	5.32 ± 0.26	25.79						

... continued

($\Delta k = 3.3 - 11 \text{ \AA}^{-1}$, He gas)									
32	Mo-Bare	S	4.3 ± 0.5	2.42 ± 0.05	9.21	0.0191	2:33:33	79 - 109.2	
		Mo	4.3 ± 0.5	3.18 ± 0.11	11.77				
		S	2.2 ± 0.3	3.77 ± 0.13	11.37				
		S	2.2 ± 0.3	4.67 ± 0.03	13.45				
		S	8.7 ± 1.0	5.29 ± 0.26	26.20				
	($\Delta k = 3.4 - 11.5 \text{ \AA}^{-1}$, He gas)								
	Mo-S50	S	4.1 ± 0.6	2.41 ± 0.04	8.88	0.0248			
		Mo	2.7 ± 0.4	3.18 ± 0.03	8.46				
		S	1.4 ± 0.2	3.73 ± 0.36	10.09				
		S	1.4 ± 0.2	4.70 ± 0.05	8.66				
S		6.8 ± 0.9	5.29 ± 0.23	23.89					
($\Delta k = 3.3 - 11 \text{ \AA}^{-1}$, He gas)									
33	Mo-Bare	S	4.4 ± 0.5	2.42 ± 0.06	9.05	0.0192	2:41:14	58.7 - 74	
		Mo	4.4 ± 0.5	3.18 ± 0.11	11.47				
		S	2.2 ± 0.3	3.77 ± 0.14	11.28				
		S	2.2 ± 0.3	4.67 ± 0.04	12.70				
		S	8.7 ± 1.0	5.29 ± 0.26	26.04				
	($\Delta k = 3.4 - 11 \text{ \AA}^{-1}$, He gas)								
	Mo-S50	S	4.2 ± 0.5	2.42 ± 0.04	9.22	0.0176			
		Mo	2.8 ± 0.3	3.17 ± 0.03	8.85				
		S	1.4 ± 0.2	3.74 ± 0.31	10.51				
		S	1.4 ± 0.2	4.70 ± 0.05	9.03				
S		4.1 ± 0.8	5.28 ± 0.22	24.02					
($\Delta k = 3.3 - 11 \text{ \AA}^{-1}$, He gas)									
34	Mo-Bare	S	4.4 ± 0.5	2.42 ± 0.06	8.89	0.0194	3:01:12	31.6 - 55.4	
		Mo	4.4 ± 0.5	3.18 ± 0.11	11.17				
		S	2.2 ± 0.3	3.76 ± 0.13	11.18				
		S	2.2 ± 0.3	4.68 ± 0.05	12.52				
		S	8.7 ± 1.0	5.28 ± 0.25	25.49				
	Mo-S50	S	4.2 ± 0.5	2.42 ± 0.04	8.88	0.0191			
		Mo	2.8 ± 0.3	3.18 ± 0.03	8.46				
		S	1.4 ± 0.2	3.73 ± 0.36	10.09				
		S	1.4 ± 0.2	4.70 ± 0.05	8.66				
		S	7.0 ± 0.8	5.29 ± 0.23	23.89				

At stage 6, Hamilton test (ref. 57) was applied by imposing k- and R-ranges on the same values in order to test two different models on the same EXAFS data independently and both of them give almost similar results (same fitting parameters)

Table 2S: Ni K-edge EXAFS fitting parameters of NiMoPILC (*in situ*)

No.	Fitting model	Back scatterer	N	R(\AA)	$\sigma^2 (\text{\AA}^2) \times 10^{-3}$	R-factor	Time-lapse	temp in $^{\circ}\text{C}$
Stage 4 ($\Delta k = 3 - 11 \text{ \AA}^{-1}$, $\text{H}_2\text{S}/\text{H}_2/\text{He}$ gasses)								
1	NiMoO ₄	O	5.2 ± 0.5	2.03 ± 0.02	7.56	0.008	1:13:11	127.8 - 159.5
		Ni	1.7 ± 0.2	3.02 ± 0.05	19.98			
		Mo	1.7 ± 0.2	3.19 ± 0.05	19.46			
		Mo	1.7 ± 0.2	3.78 ± 0.0	11.94			
2	NiMoO ₄	O	5.2 ± 0.5	2.02 ± 0.02	7.95	0.0112	1:15:48	176.3 - 193.3
		Ni	1.7 ± 0.2	3.01 ± 0.04	20.55			
		Mo	1.7 ± 0.2	3.2 ± 0.06	19.61			
		Mo	1.7 ± 0.2	3.77 ± 0.07	11			

... continued

3	NiMoO ₄	O	5.1 ± 0.5	2.02 ± 0.02	8.43	0.0086	1:23:38	210.1 – 294.7
		Ni	1.7 ± 0.2	3.01 ± 0.05	19.01			
		Mo	1.7 ± 0.2	3.19 ± 0.05	19.65			
		Mo	1.7 ± 0.2	3.78 ± 0.07	14.52			
4	NiMoO ₄	O	5.2 ± 0.6	2.01 ± 0.01	9.93	0.0118	1:26:14	311.6 – 328.3
		Ni	1.7 ± 0.2	3.02 ± 0.05	25.04			
		Mo	1.7 ± 0.2	3.21 ± 0.07	18.95			
		Mo	1.7 ± 0.2	3.71 ± 0.01	15.38			
(Δk = 3 – 11.6 Å ⁻¹ , H ₂ S/H ₂ /He gasses)								
5	NiMoO ₄	O	5.4 ± 0.7	2.01 ± 0.0	9.89	0.0169	1:27:33	345.1
		Ni	1.8 ± 0.3	3.02 ± 0.05	25.79			
		Mo	1.8 ± 0.3	3.18 ± 0.04	14.83			
		Mo	1.8 ± 0.3	3.74 ± 0.04	20.03			
6	NiMoO ₄	O	5.6 ± 0.9	1.99 ± 0.01	11.34	0.02	1:28:51	362
		Ni	1.9 ± 0.3	3.05 ± 0.08	27.62			
		Mo	1.9 ± 0.3	3.20 ± 0.06	17.94			
		Mo	1.9 ± 0.3	3.69 ± 0.01	16.48			
(Δk = 3 – 12 Å ⁻¹ , H ₂ S/H ₂ /He gasses)								
7	NiMoO ₄	O	5.8 ± 0.5	2.01 ± 0.01	11.62	0.0096	1:30:09	378.9
		Ni	1.9 ± 0.2	3.01 ± 0.05	26.17			
		Mo	1.9 ± 0.2	3.18 ± 0.04	19.66			
		Mo	1.9 ± 0.2	3.77 ± 0.06	14.83			
8	NiMoO ₄	O	3.5 ± 0.4	2.02 ± 0.02	6.26	0.0197	1:31:28	395.4
		Ni	1.2 ± 0.1	3.03 ± 0.06	21.3			
		Mo	1.2 ± 0.1	3.23 ± 0.09	11.33			
		Mo	1.2 ± 0.1	3.71 ± 0.01	15.12			
Stage 5 (Δk = 2.8 – 10 Å ⁻¹ , H ₂ S/H ₂ /He gasses)								
9	NiMoO ₄	O	4.8	1.99 ± 0.01	11.18	0.0199	1:34:51	414.2
		Ni	1.6	3.0 ± 0.03	16.69			
		Mo	1.6	3.16 ± 0.02	17.64			
(Δk = 3 – 11 Å ⁻¹ , H ₂ S/H ₂ /He gasses)								
10	NiO Ni ₃ S ₂	O	2	1.99 ± 0.1	3.79	0.0197	1:36:41	418.1
		S	1.2	2.3 ± 0.05	23.06			
		Ni	1.2	2.51 ± 0.01	12.18			
11	NiO Ni ₃ S ₂	O	4.5	2.07 ± 0.02	12.13	0.0091	1:39:18	419.5
		S	1.6	2.17 ± 0.08	10.14			
		Ni	1.6	2.55 ± 0.06	19.85			
		S	1.6	3.62 ± 0.05	12.38			
(Δk = 3 – 10.8 Å ⁻¹ , H ₂ S/H ₂ /He gasses)								
12	NiO Ni ₃ S ₂	O	5.5	2.05 ± 0.04	14.76	0.0183	1:41:15	421.9
		S	2	2.16 ± 0.09	12.5			
		Ni	2	2.54 ± 0.04	22.65			
		S	2	3.58 ± 0.09	14.21			
(Δk = 3 – 11 Å ⁻¹ , H ₂ S/H ₂ /He gasses)								
13	NiO Ni ₃ S ₂	O	5.5	2.1 ± 0.01	19.99	0.0151	1:44:31	423.2
		S	2.3	2.2 ± 0.05	11.28			
		Ni	2.3	2.55 ± 0.05	22.46			
		S	2.3	3.62 ± 0.06	13			
14	NiO Ni ₃ S ₂	O	5.6 ± 0.4	2.04 ± 0.05	6	0.0133	1:47:08	424.1
		S	2.8	2.07 ± 0.18	13.65			
		Ni	2.8	2.58 ± 0.08	20.99			
		S	2.8	3.66 ± 0.01	17.34			

... continued

15	Ni-Oxy50		$(\Delta k = 3.5 - 11 \text{ \AA}^{-1}, \text{H}_2\text{S}/\text{H}_2/\text{He gasses})$				0.0175	1:49:45	424.7
		O	0.8	1.5 ± 0.23	12.91				
		S	3.2	2.23 ± 0.01	11.55				
		Mo	1.6	2.58 ± 0.31	16.56				
		Ni	1.6	2.98 ± 0.17	12.33				
16	Ni-Oxy50		$(\Delta k = 3 - 10 \text{ \AA}^{-1}, \text{H}_2\text{S}/\text{H}_2/\text{He gasses})$				0.0199	1:52:21	425 - 425.2
		O	0.6	1.35 ± 0.38	19.21				
		S	2.4	2.22 ± 0.0	7.24				
		Mo	1.2	3.19 ± 0.30	11.13				
		Ni	1.2	2.95 ± 0.2	21.85				
17	Ni-Oxy50		$(\Delta k = 3.5 - 12 \text{ \AA}^{-1}, \text{H}_2\text{S}/\text{H}_2/\text{He gasses})$				0.0171	1:57:35	425.3
		O	0.7	2.03 ± 0.3	23.02				
		S	2.9	2.2 ± 0.02	10.78				
		Mo	1.4	2.77 ± 0.12	13.32				
		Ni	1.4	3.3 ± 0.15	14.39				
18	NiMoS ($\bar{1}010$)		$(\Delta k = 3.7 - 11 \text{ \AA}^{-1}, \text{H}_2\text{S}/\text{H}_2/\text{He gasses})$				0.0094	2:00:12	425.4 - 426.3
		S	3.2 ± 0.4	2.19 ± 0.15	10.63				
		Mo	1.1 ± 0.1	2.74 ± 0.06	6.88				
		Mo	1.1 ± 0.1	2.93 ± 0.07	7.62				
		S	2.1 ± 0.3	3.53 ± 0.12	9.66				
19	NiMoS ($\bar{1}010$)		$(\Delta k = 3.4 - 11 \text{ \AA}^{-1}, \text{H}_2\text{S}/\text{H}_2/\text{He gasses})$				0.0163	2:12:18	426.1 - 426.6
		S	2.7 ± 0.4	2.19 ± 0.15	8.16				
		Mo	0.9 ± 0.1	2.76 ± 0.04	5.34				
		Mo	0.9 ± 0.1	2.94 ± 0.06	6.93				
		S	1.8 ± 0.2	3.52 ± 0.12	8.60				
20	Ni-Bare		Stage 6 ($\Delta k = 3 - 11 \text{ \AA}^{-1}, \text{He gas}$)				0.0129	2:38:04	199.6 - 427.2
		S	2.4 ± 0.3	2.2 ± 0.01	6.62				
		Mo	1.2 ± 0.1	2.76 ± 0.01	9.03				
		Ni	1.2 ± 0.1	3.14 ± 0.01	8.45				
			S	1.2 ± 0.1	3.52 ± 0.03	1.16			
	NiMoS ($\bar{1}010$)	S	2.7 ± 0.3	2.2 ± 0.16	7.33	0.0102			
		Mo	0.9 ± 0.1	2.78 ± 0.02	4.30				
		Mo	0.9 ± 0.1	2.96 ± 0.04	4.43				
S		1.8 ± 0.2	3.52 ± 0.12	5.91					
21	Ni-Bare	S	2.7 ± 0.3	2.2 ± 0.02	5.88	0.0146	2:57:39	86.2 - 188.7	
		Mo	1.3 ± 0.2	2.76 ± 0.0	7.87				
		Ni	1.3 ± 0.2	3.12 ± 0.03	7.77				
		S	1.3 ± 0.2	3.51 ± 0.04	0.91				
	NiMoS ($\bar{1}010$)	S	3.0 ± 0.3	2.21 ± 0.06	6.64	0.0153			
		Mo	1.0 ± 0.1	2.76 ± 0.04	3.07				
		Mo	1.0 ± 0.1	2.95 ± 0.06	3.35				
		S	2.0 ± 0.2	3.51 ± 0.13	5.51				
22	Ni-Bare	S	2.7 ± 0.4	2.21 ± 0.02	5.64	0.0175	3:17:14	42 - 81.2	
		Mo	1.4 ± 0.2	2.75 ± 0.0	7.47				
		Ni	1.4 ± 0.2	3.12 ± 0.03	8.13				
		S	1.4 ± 0.2	3.51 ± 0.04	0.97				
	NiMoS ($\bar{1}010$)	S	3.0 ± 0.4	2.21 ± 0.17	6.18	0.0185			
		Mo	1.0 ± 0.1	2.76 ± 0.04	2.87				
		Mo	1.0 ± 0.1	2.94 ± 0.06	3.61				
		S	2.0 ± 0.2	3.51 ± 0.13	5.08				

... continued

23	Ni-Bare	S	2.8 ± 0.4	2.21 ± 0.02	5.5	0.0177	3:43:13	29.6 - 40.4
		Mo	1.4 ± 0.2	2.75 ± 0.0	7.36			
		Ni	1.4 ± 0.2	3.12 ± 0.03	7.8			
		S	1.4 ± 0.2	3.51 ± 0.04	0.61			
	NiMoS (1010)	S	3.0 ± 0.3	2.22 ± 0.17	5.79	0.0155		
		Mo	1.0 ± 0.1	2.76 ± 0.04	2.86			
		Ni	1.0 ± 0.1	2.94 ± 0.06	3.53			
		S	2.0 ± 0.2	3.52 ± 0.13	4.88			

At stage 6, Hamilton test [57] was applied by imposing k- and R-ranges on the same values in order to fit two different models on the same EXAFS data independently and both of them give almost similar results (same fitting parameters)

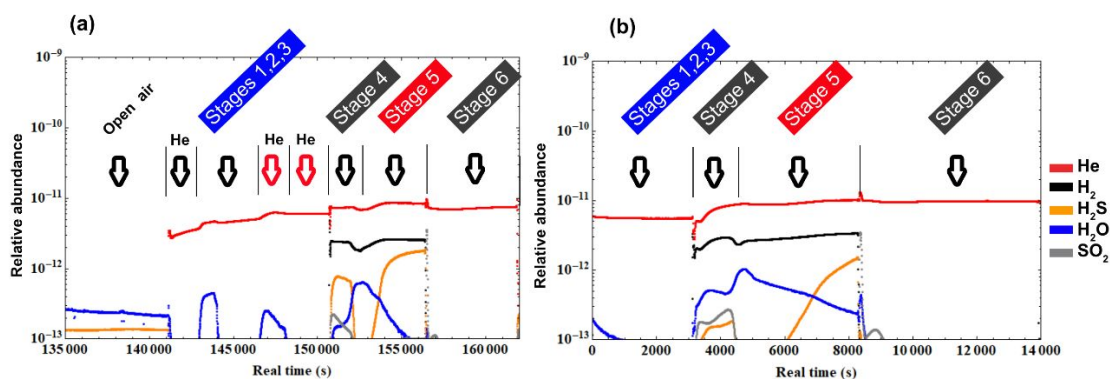


Figure 1S: Distribution profile of gas products (H_2O , SO_2) and inputs (He , H_2 , H_2S) during *in situ* (a) Mo and (b) Ni K-edge XAS measurement using MS

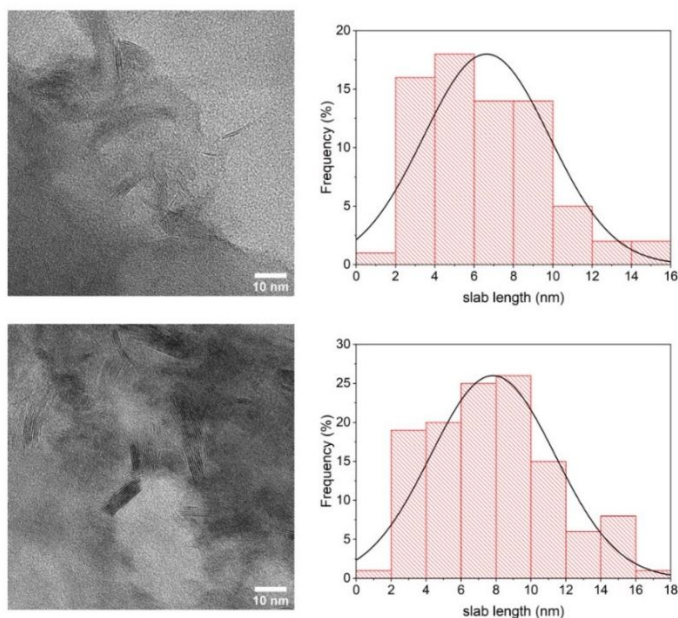


Figure 2S: HRTEM images (left) at two different locations and their respective slab length distributions (right) of sulfided $\text{NiMoS}_2/\text{Al-PILC}$ catalyst.

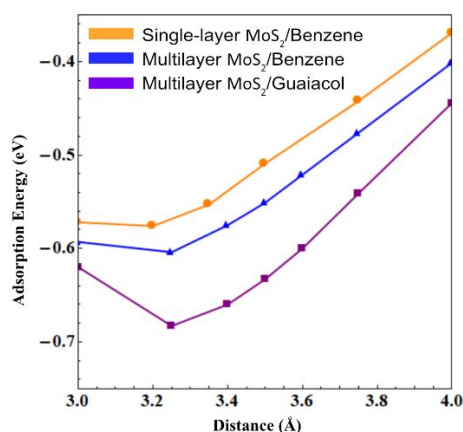


Figure 35: Benzene and guaiacol adsorption on the basal plane of MoS₂ in planar configuration. The distance is from the center of mass of benzene and guaiacol to the z position of the top sulfur layer

Table 3S: Calculated vibrational frequencies (cm⁻¹) of guaiacol adsorbed on several NiMoS₂ sites

	Mo-Bare	Ni-Bare	Mo-S50	NiMoS ($\bar{1}$ 010)	Horiz-basal	Vert-basal	INS (ref. 25)
$\nu(\text{C-C})$	1512	1499, 1579, 1601	1499, 1578, 1620	1469, 1590, 1615	1512, 1593, 1608	1505, 1593, 1612	-
$\gamma(\text{CH}_3)$	1459	1451, 1458	1450, 1458	1455	-	1461	1463
$\nu(\text{C-C}) + \gamma(\text{CH}_3)$	1443, 1450	1446	1449	1448	1446, 1459	1452	-
$\gamma(\text{CH}_3)$	-	-	-	-	1439	1447	-
$\delta(\text{CH}_3)$	-	1434	1436	1425, 1435	1429	1430	-
$\nu(\text{C-C}) + \delta(\text{COH})$	1415, 1423	-	-	-	-	-	-
$\nu(\text{C-C})$	1335, 1366	1362	1368	1366	1397	1390	1378
$\delta(\text{C-H})$	1263	1290	1293	1296	1295	1297	-
$\nu(\text{C-OH}) + \nu(\text{C-OCH}_3)$	-	-	-	-	1272	1236, 1273	-
$\nu(\text{C-OCH}_3)$	1205	1266	1270	-	1243	-	-
$\nu(\text{C-OH})$	1187	1221	1191	1251	-	-	-
$\nu(\text{C-OCH}_3)$	-	-	-	1205	-	-	-
$\delta(\text{CH}_3)$	1174	1180	1180	1173	1179	1184	-
$\delta(\text{C-H})$	-	1169	1169	1168	1167	1164	1164
$\delta(\text{CCC})$ ip	-	1156	1159	1157	1154	-	-
$\nu(\text{C-OH})$	-	-	1148	-	-	-	-
$\delta(\text{O-CH}_3)$	1143	1142	1140	1142	1139	1142	1043
$\delta(\text{CCC})$ ip	1140	-	-	1102	1101	1100	-
$\nu(\text{C-OH})$	1089	1096	1085	-	-	-	-
$\delta(\text{CCC})$ ip	990, 1033	1055	1059	1050	1055	1069	-
$\delta(\text{CCC})$ ip + $\nu(\text{O-CH}_3)$	983	1028	1025	1009	1041	1042	-
$\tau(\text{C-H})$	-	-	-	-	-	953	-
$\delta(\text{CCC})$ oop	826, 898	833, 918, 965	827, 912, 965	830, 913, 963	895, 947	894	846, 926, 963
$\delta(\text{CCC})$ ip	-	891	-	824	832	830	-
$\delta(\text{CCC})$ oop	-	-	-	-	821	816	-
$\delta(\text{CCC})$ ip	787, 788	751	750, 814	771	764	765	752

$\delta(\text{C-H})$	-	748	741	742	745	746	-
$\delta(\text{CCC})$ oop	747	713	-	-	721	718	-
$\delta(\text{CCC})$ ip	728	-	-	-	-	-	-
$\delta(\text{C-OH})$	692	-	676	-	-	-	-
$\delta(\text{CCC})$ oop	611	-	-	-	583	-	-
$\delta(\text{CCC})$ ip	557	574	581	600	-	584	557
$\delta(\text{CCC})$ oop	-	559	558	558	570	571	-
$\delta(\text{C-OH})$	-	548	-	-	-	-	-
$\rho(\text{C-O})$	-	-	532	538	524	524	536
$\delta(\text{CCC})$ ip	471, 476, 516	492	503	508	498	492	495
$\delta(\text{CCC})$ oop	-	461	468	447	471	467	461
$\delta(\text{C-OH})$	-	-	-	437	-	-	-
$\gamma(\text{C-O})$	-	-	-	412	-	-	-
$\delta(\text{CCC})$ oop	403	-	-	-	-	-	-
$\delta(\text{C-OH})$	-	-	-	-	382	370	-
$\nu(\text{Mo-O}) + \nu(\text{Mo-C})$	356	-	-	-	-	-	-
$\gamma(\text{C-O})$	-	334	361	-	350	337	-
$\delta(\text{CCC})$ oop	302, 333	323	344	314	317	319	314, 346
$\tau(\text{O-CH}_3)$	-	271	268	-	-	266	-
$\gamma(\text{C-O})$	-	-	258	268	-	-	-
$\nu(\text{Mo-O})$	254	-	-	-	-	-	-
$\tau(\text{O-CH}_3)$	234	-	-	243	249	-	252
$\gamma(\text{C-O})$	227	231	-	-	233	227	-
$\tau(\text{O-CH}_3)$	-	-	221	-	-	-	-
$\tau(\text{C-O})$	-	211	-	206	195	192	206
$\delta(\text{O-CH}_3)$	173	-	-	190	169	126	-
$\delta(\text{CCC})$ oop	137	138	149	-	-	-	147

ν ---stretching, δ ---bending, γ ---scissoring, ω ---wagging, τ ---twisting, torsion, ρ ---rocking, oop---out-of-plane, ip---in-plane. Vibrational mode descriptions obtained using animations in Chemcraft.